Entanglement and Charge-Sharpening Transitions in U(1) Symmetric Monitored Quantum Circuits

Utkarsh Agrawal,[1] Aidan Zabalo,[2] Kun Chen,[3] Justin H. Wilson,[2,4,5] Andrew C. Potter,[6,7] J. H. Pixley,[2,8,3] Sarang Gopalakrishnan,[9,10] and Romain Vasseur[1]

[1]*Department of Physics, University of Massachusetts, Amherst, Massachusetts 01003, USA*
[2]*Department of Physics and Astronomy, Center for Materials Theory, Rutgers University, Piscataway, New Jersey 08854, USA*
[3]*Center for Computational Quantum Physics, Flatiron Institute, 162 5th Avenue, New York, New York 10010, USA*
[4]*Department of Physics and Astronomy, Louisiana State University, Baton Rouge, Louisiana 70803, USA*
[5]*Center for Computation and Technology, Louisiana State University, Baton Rouge, Louisiana 70803, USA*
[6]*Department of Physics, University of Texas at Austin, Austin, Texas 78712, USA*
[7]*Department of Physics and Astronomy, and Quantum Matter Institute, University of British Columbia, Vancouver, British Columbia, Canada V6T 1Z1*
[8]*Department of Physics, Princeton University, Princeton, New Jersey 08544, USA*
[9]*Department of Physics, The Pennsylvania State University, University Park, Pennsylvania 16802, USA*
[10]*Department of Electrical and Computer Engineering, Princeton University, Princeton, New Jersey 08544, USA*

(Received 14 September 2021; accepted 12 August 2022; published 7 October 2022)

Monitored quantum circuits can exhibit an entanglement transition as a function of the rate of measurements, stemming from the competition between scrambling unitary dynamics and disentangling projective measurements. We study how entanglement dynamics in nonunitary quantum circuits can be enriched in the presence of charge conservation, using a combination of exact numerics and a mapping onto a statistical mechanics model of constrained hard-core random walkers. We uncover a charge-sharpening transition that separates different scrambling phases with volume-law scaling of entanglement, distinguished by whether measurements can efficiently reveal the total charge of the system. We find that while Rényi entropies grow sub-ballistically as $\sqrt{t}$ in the absence of measurement, for even an infinitesimal rate of measurements, all average Rényi entropies grow ballistically with time $\sim t$. We study numerically the critical behavior of the charge-sharpening and entanglement transitions in U(1) circuits, and show that they exhibit emergent Lorentz invariance and can also be diagnosed using scalable local ancilla probes. Our statistical mechanical mapping technique readily generalizes to arbitrary Abelian groups, and offers a general framework for studying dissipatively stabilized symmetry-breaking and topological orders.

DOI: 10.1103/PhysRevX.12.041002

Subject Areas: Condensed Matter Physics, Quantum Information, Statistical Physics

I. INTRODUCTION

The dynamics of quantum information has become a central theme across multiple branches of physics ranging from condensed matter and atomic physics to quantum gravity [1–5]. Of particular recent interest is the exploration of entanglement dynamics in open quantum systems, motivated by the advent of noisy intermediate-scale quantum simulators [6]. The dynamics of an open system monitored by an external observer or coupled to its environment consists of two competing processes: unitary evolution, which generates entanglement and generically leads to chaotic dynamics [7–12], and nonunitary operations resulting from measurements and noisy couplings to the environment, that tend to irreversibly destroy quantum information stored in the system by revealing it to the environment.

A minimal model that captures these competing processes consists of a quantum circuit made up of random unitary gates interlaced with local projective measurements. Remarkably, this minimal model undergoes a dynamical

phase transition as the rate of measurements is increased. This transition occurs in individual quantum trajectories (i.e., the state of the system conditional on a set of measurement outcomes), and separates two phases where typical trajectories have very different entanglement properties [13,14]. When measurements are frequent enough, they rapidly extract quantum information from any initial state and collapse it into a weakly entangled pure state. Below a critical measurement rate, however, initial product states grow highly entangled over time, while initial mixed states remain mixed for extremely long times. In this "entangling" phase, unitary dynamics scrambles quantum information into nonlocal degrees of freedom that can partly evade local measurements. These nonlocal degrees of freedom span a decoherence-free subspace in which the dynamics is effectively unitary [15–18]: this subspace can be regarded as the code space of a quantum error correcting code. The effective size of the protected subspace vanishes at the measurement-induced phase transition. The critical properties of the measurement-induced transition are still under investigation, but key qualitative features of the transition including the emergence of conformal invariance are by now well established [19–22]. Meanwhile, different variants of this transition have been investigated involving various ensembles of gates, circuit geometries, etc., establishing that such transitions are generic aspects of the quantum trajectories of open systems [13–50].

Given the central role of scrambling in the measurement-induced transition, it is natural to ask how the transition (and the entangling phase) is affected if one constrains the scrambling dynamics by imposing symmetries or conservation laws. Even in the absence of measurements, conservation laws severely constrain the scrambling of local operators [11,12,51]. Moreover, conservation laws can parametrically slow down entanglement growth. For example, the dynamics of the Rényi entropies,

$$S_n = \frac{1}{1-n} \ln \mathrm{tr} \rho_A^n \tag{1}$$

(with ρ_A the reduced density matrix of a subsystem A), in systems with a conserved charge have been shown to grow sub-ballistically as $S_{n>1} \sim \sqrt{t}$ [52–56], while the von Neumann entropy remains linear in time $S_1 \sim t$. These results suggest that slow hydrodynamic modes might fundamentally alter not just the nature of the measurement-induced phase transition but also the nature of the entangling phase. General arguments and numerical studies of both Clifford and noninteracting fermion circuits give evidence that symmetries enable distinct phases of volume-law-entangled dynamics [47], which would be fundamentally impossible in thermal equilibrium. Despite this work, many fundamental questions about the nature and phase structure and universal properties of measurement-induced phases and critical phenomena in volume-law-entangled matter with symmetries remain unanswered—in large part due to the absence of tractable analytic and numerical approaches for analyzing disorder-averaged quantum circuits with generic (computationally universal) gate sets.

In this work we study the many-body dynamics of monitored quantum circuits with a conserved charge [or equivalently a U(1) symmetry] and introduce a systematic tool to analytically perform the proper averaging over random gates and measurement outcomes with well-controlled approximations for general family of monitored circuit models with universal gates. This technique enables efficient numerical analysis of large-scale monitored random circuits and opens the door to potential analytic analysis using well-developed statistical mechanics and field-theoretic tools [57]. Using this approach, we show that charge-conserving monitored random circuits exhibit not only a measurement-induced entanglement transition but also a new type of "charge-sharpening" transition that separates two distinct entangling phases. These two phases are distinguished by whether it is easy or hard (in a way we will make precise below) for measurements to reveal the charge of the system. In the "charge-fuzzy" phase, there are large charge fluctuations even *conditional* on the measurement history; i.e., the history of measurement outcomes does not suffice to fix the charge profile. In the "charge-sharp" entangling phase, by contrast, the measurement outcomes fix the charge distribution. The charge-sharp phase is nevertheless highly entangled because of the scrambling of neutral degrees of freedom. We find that both the entanglement transition and the charge-sharpening transition are Lorentz invariant, with a dynamical exponent $z = 1$. This ballistic dynamics may seem surprising in light of the diffusive growth of Rényi entropies in the absence of measurements. However, we give general arguments that, for any finite measurement rate $p > 0$, all Rényi entropies grow linearly in time, $S_n \sim t$.

Our conclusions are supported by exact numerics on Haar-random U(1) monitored circuits, and by a replica statistical mechanics model [19,20] obtained from the study of a U(1) symmetric qubit degree of freedom coupled to a d-dimensional qudit. Remarkably, in the limit $d \to \infty$, we are able to analyze the replica limit analytically, and the contributions to entanglement from the qubit and qudit degree of freedom decouple. This enables us to study the entanglement dynamics of the qubit directly in this limit by simulating an effective statistical mechanics model of a symmetric exclusion process constrained by the measurements and entanglement cuts. We also discuss scalable probes of the charge-sharpening transition using ancilla qubits and find evidence for a new universality class for the charge-sharpening transition in the limit of small local Hilbert space dimension.

The plan of the rest of the paper is as follows. In Sec. II we specify the models we have explored and present some general considerations on their steady-state phases and dynamics. In Sec. III we present numerical results for U(1) symmetric qubit chains. In Sec. IV we present a tractable

limit in which the model can be mapped onto the statistical mechanics of constrained random walkers. In Sec. V we present numerical results for the transfer matrix of this statistical model. Finally, in Sec. VI we summarize our results and discuss their broader implications. In particular, we note that these methods can be readily generalized to general Abelian symmetry groups, as detailed in Appendix B, where we leverage duality relations to discuss implications for systems with highly entangled phases with symmetry-breaking and topological orders.

II. OVERVIEW OF RESULTS

In this section, we introduce a family of U(1) symmetric circuits and present some general observations concerning their steady-state phase structure and entanglement dynamics. The numerical evidence supporting these observations is presented in Secs. III and V.

A. Models

Following Ref. [12], we consider a one-dimensional chain in which each site hosts a two-level system ("qubit") and a d-level system ("qudit"); i.e., the on-site Hilbert space is $\mathbb{C}^2 \otimes \mathbb{C}^d$ for $d > 1$ and $\mathbb{C}^2$ for $d = 1$. The dynamics will consist of local unitary gates and measurements, which are chosen to conserve the U(1) charge,

$$\mathcal{Q} \equiv \sum_i \mathfrak{q}_i \otimes \mathbb{I}_i, \tag{2}$$

where $\mathfrak{q}_i = (\sigma_i^z + 1)/2$ is acting on the ith site of the chain of length L and $\mathbb{I}$ is the identity matrix on the qudits. These chains evolve under (i) unitary 2-qubit gates, acting on nearest neighbor sites, which conserve the global charge $\mathcal{Q}$, and (ii) single-site projective measurements in which the qubit is measured in its Z basis and the qudit is simultaneously measured in some reference basis [58]. At each time step, a given site is measured with probability p; for specificity, we assume that when this happens both the qubit *and* the qudit are measured, so the measurement acts on that site as a rank-1 projector. The symmetry-preserving two-site unitary gates are arranged in a brickwork geometry and take the form

$$U_{i,i+1} = \begin{pmatrix} U^0_{d^2\times d^2} & 0 & 0 \\ 0 & U^1_{2d^2\times 2d^2} & 0 \\ 0 & 0 & U^2_{d^2\times d^2} \end{pmatrix}, \tag{3}$$

where i labels a site, $U^{\mathfrak{q}}_{D\times D}$ is a unitary matrix of size $D \times D$ acting on the charge $\mathfrak{q}_1 + \mathfrak{q}_2 = \mathfrak{q} \in \{0, 1, 2\}$ sector (a local charge is defined to take values 0 and 1), and D is the dimension of the Hilbert space of the charge sector. Each matrix is drawn independently from the Haar-random ensemble of unitary matrices of the appropriate size.

We present numerical results for this class of circuits in two limits. First, we consider the limit $d = 1$, where there is no qudit degree of freedom, and one simply has a chain of qubits interacting via gates that conserve the charge $\mathcal{Q}$. In this limit, we obtain numerical results by direct time evolution. Second, we consider the complementary limit $d = \infty$, in which we can map the problem to a statistical mechanics model and explicitly write down a transfer matrix that generates the observables of interest. The phase diagrams in the two complementary limits are similar.

The qubit-only ($d = 1$) model is directly realizable in existing quantum processors. The $d > 1$ model is perhaps less natural experimentally, but could be realized in circuit quantum electrodynamics setups [59] in which superconducting transmon qubits are coupled to multilevel superconducting cavities (qudits), or by blocking multiple qubits together (e.g., $d = 2$ could be realized as a two-leg ladder of qubits). Regardless of experimental implementation, we expect the $d > 1$ models to capture the generic universal behavior of phases and transitions, while allowing greater theoretical control in the large-d limit.

B. Observables and averaging

For a given choice of unitary gates and measurement locations $\mathbf{X}$ (in spacetime), the unitary-measurement dynamics can be described in terms of quantum trajectories $\rho_{\mathbf{m}}(t) = K_{\mathbf{m}}\rho K_{\mathbf{m}}^\dagger$. Here $\mathbf{m}$ denotes a "quantum trajectory," associated with a fixed configuration of measurement locations $\mathbf{X}$ and measurement outcomes $\mathcal{M}(\mathbf{X})$. We will write $\mathbf{m} = \{\mathbf{X}, \mathcal{M}(\mathbf{X})\}$. The Kraus operators $K_{\mathbf{m}}$ consist of random unitary gates and projection operators onto the measurement outcomes $\mathcal{M}(\mathbf{X})$, and we have $\sum_{\{\mathcal{M}(\mathbf{X})\}} K_{\mathbf{m}}^\dagger K_{\mathbf{m}} = \mathbb{I}$.

We will be concerned with general properties of the single-trajectory state $\rho_{\mathbf{m}} \equiv K_{\mathbf{m}}\rho K_{\mathbf{m}}^\dagger$. [As a concrete example, consider the purity $\Pi_{\mathbf{m}} = \mathrm{Tr}(\rho_{\mathbf{m}}^2)/(\mathrm{Tr}\rho_{\mathbf{m}})^2$.] We then average over quantum trajectories, weighting each set of measurement outcomes by its probability of occurrence, i.e., the Born probability $p_{\mathbf{m}} = \mathrm{Tr}(\rho_{\mathbf{m}})$. Finally, we average the answers across the ensemble of quantum circuits.

A few comments are in order here.

(1) For an initially pure state $|\psi\rangle$ the Born probability takes the familiar form $p_{\mathbf{m}} = \|K_{\mathbf{m}}|\psi\rangle\|^2$; i.e., it is just the norm of the projected state. For a series of measurements interspersed with unitary gates, one can pick each measurement outcome based on the Born probability or *equivalently* apply a set of projectors at random and evaluate the probability of the entire measurement history by computing the norm of the state at the end of the trajectory.

(2) There are four different types of average that we consider here: (i) the quantum expectation value of an observable A in a single trajectory $\rho_{\mathbf{m}}$, namely, $\mathrm{Tr}(A\rho_{\mathbf{m}})/\mathrm{Tr}\rho_{\mathbf{m}}$, which we will write as $\langle A\rangle_{\mathbf{m}}$; (ii) the

(Born-weighted) average of a single-trajectory function, such as purity or entanglement entropy, over quantum trajectories (measurement outcomes); (iii) the average over unitary gates, chosen with Haar measure; and (iv) the average over spacetime points where the measurements occur (measurement locations). In much of this work, we present results for which averages (ii)–(iv) have been done. We will use the notation $[\cdot]$ for this full average. At some points it will be useful to separate these averages. In these cases we will use the explicit notations $\sum_{\{\mathcal{M}(\mathbf{X})\}}(\cdot)$, $\mathbb{E}_U(\cdot)$, and $\mathbb{E}_{\mathbf{X}}(\cdot)$ for averages over measurement outcomes, gates, and measurement locations, respectively. We will also use a shorthand notation $\mathbb{E}_{\mathbf{m}} \equiv \sum_{\mathbf{m}} p_{\mathbf{m}}(\ldots)$ to denote summation over all possible measurement locations $\mathbf{X}$ including appropriate probability factors of p and $1-p$, and over all measurement outcomes $\mathcal{M}(\mathbf{X})$, including the associated Born probability factor $p_{\mathbf{m}}$.

(3) It is crucial that the quantities of interest to us are *nonlinear* functions of $\rho_{\mathbf{m}}$ [14], such as $\Pi_{\mathbf{m}}$. To see the significance of this, let us compare the quantity $\Pi_{\mathbf{m}}$ to that of some simple expectation value. In $\rho_{\mathbf{m}}$, the expectation value of a local operator A would be $\mathrm{Tr}(A\rho_{\mathbf{m}})/\mathrm{Tr}\rho_{\mathbf{m}}$. Averaging this over trajectories (measurement outcomes) with the Born probabilities would simply give infinite temperature behavior [60]: $\sum_{\{\mathcal{M}(\mathbf{X})\}}(p_{\mathbf{m}}\langle A\rangle_{\mathbf{m}}) = \sum_{\{\mathcal{M}(\mathbf{X})\}}\mathrm{Tr}(A\rho_{\mathbf{m}}) = \mathrm{Tr}(A\rho(t)) \approx \mathrm{Tr}(A)/\mathrm{Tr}(1)$, where $\rho(t) = \sum_{\{\mathcal{M}(\mathbf{X})\}} \times K_{\mathbf{m}}\rho K_{\mathbf{m}}^{\dagger}$ describes the dynamics of the density matrix in the case where the environment does not monitor or keep track of the measurement outcomes. By contrast, $\sum_{\{\mathcal{M}(\mathbf{X})\}}\Pi_{\mathbf{m}}p_{\mathbf{m}} = \sum_{\{\mathcal{M}(\mathbf{X})\}}\mathrm{Tr}(\rho_{\mathbf{m}}^2)/\mathrm{Tr}\rho_{\mathbf{m}}$, which cannot simply be written in terms of $\rho(t)$. The averaged density matrix $\rho(t)$ is blind to measurement transitions; only nonlinear functions of single-trajectory wave functions detect it.

C. Results

In the following, we unveil a charge-sharpening transition that takes place before the entanglement transition in two distinct models of monitored U(1) symmetric random quantum circuits. Our main results are summarized in Fig. 1 and discussed in more detail below.

1. Entanglement transition

A general feature of unitary-projective circuits is the presence of an *entanglement transition*, separating a phase where initially unentangled states develop volume-law entanglement from one where their entanglement remains area law at all times. We briefly review the general properties of this transition and discuss how they are modified by the presence of a conservation law.

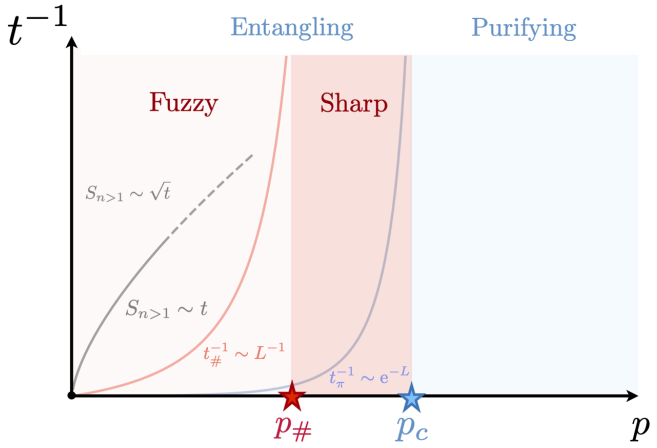

FIG. 1. Phase diagram and crossover timescales in U(1) symmetric monitored quantum circuits. Our numerical results indicate that there are two distinct phases in the entangling (volume-law) regime $p < p_c$, separated by a charge-sharpening critical point as $p = p_{\#}$. In the charge-fuzzy phase ($p < p_{\#}$), we identify three relevant timescales in the dynamics: For a large enough system, first (1) average Rényi entropies crossover from diffusive $[S_{n>1}] \sim \sqrt{t}$ to ballistic $\sim t$ scaling over a timescale $\sim p^{-3/2}$, then (2) charge sharpens after the crossover timescale $t_{\#} \sim L$, and finally (3) the system purifies over a much longer timescale $t_{\pi} \sim \mathrm{e}^{L}$.

This transition occurs at some critical measurement rate p_c. In the volume-law phase, the half-system entanglement entropy grows linearly in time and saturates on timescales $t \sim L$. At times $t > L$, the entanglement entropy (averaged over circuits and trajectories) reaches a steady-state value $[S(L/2)] = cL$, where c is a constant that decreases continuously to zero at p_c. At $p = p_c$, we have that $[S_n(L/2)] = \alpha_n \log L$, where α_n (which generally depends on the Rényi index n) is part of the universal critical data [14,28].

An equivalent way to understand the entanglement transition is as a "purification transition" for an initially mixed state [16]. For $p < p_c$, an initially mixed state for a system of size L evolves to a pure state on a timescale $t_{\pi} \sim \exp(L)$, whereas for $p > p_c$, purification happens on a timescale that grows sublinearly in L. If one takes the limits $L \to \infty$, $t/L = \mathrm{const}$, the purity of an initially mixed state for $p < p_c$ is essentially constant in time; i.e., the steady state is defined to be at early times compared with the slow purification dynamics for $p < p_c$.

The purity of an initially mixed state on timescales $t \sim L$ can be used to define an effective order parameter for the volume-law phase, as follows [27,28]. Consider evolving a pure state along some trajectory until times $t \sim L$, and then entangling some local degree of freedom with an ancilla qubit. The reduced density matrix of the system is now a rank-2 mixed state. For $p < p_c$, this mixed state remains mixed for an exponentially long time. Therefore, by evolving for another $t \sim L$ and then measuring the

entanglement entropy of the ancilla (which is equivalent to measuring the purity of the system density matrix in this setup), one can extract a local order parameter for the volume-law phase [27]. By studying the correlations of this local order parameter—e.g., by coupling in two ancillas at distinct spacetime points and tracking their mutual information—it was established [in the absence of the U(1) symmetry] that the critical theory has an emergent Lorentz invariance with dynamical scaling exponent $z = 1$.

One of our results is to locate and characterize this entanglement transition in the presence of the U(1) conservation law. In the $d \to \infty$ limit, we find that $p_c = 1/2$, exactly as in the absence of a conservation law. Moreover, the entanglement transition corresponds to a percolation transition. For $d = 1$, we find that $p_c = 0.105(3)$ moves to substantially lower measurement rate than in the generic circuit without a conservation law ($p_c^{\mathrm{Haar}} \approx 0.17$ [28]). The correlation length exponent $\nu = 1.32(6)$ is close to the percolation value $4/3$, but the coefficients α_n differ from the percolation value as well as the value for Haar-random circuits without a U(1) symmetry. Finally, we find compelling numerical evidence that the dynamical scaling $z = 1$ holds at this critical point. That this holds regardless of the diffusive ($z = 2$) dynamics of the U(1) conserved charge is perhaps puzzling at first sight. We return below to the resolution of this puzzle.

2. Charge-sharpening transition

In addition to changing the critical properties of the entanglement transition at p_c, the conservation law gives rise to a *distinct* charge-sharpening transition at a measurement rate $p_\#$ inside the volume-law phase. The charge-sharpening transition separates a charge-sharp phase for $p > p_\#$, in which the measurements along a typical trajectory can rapidly collapse an initial pure superposition (or mixture) of different charge sectors, and a charge-fuzzy phase where this collapse is parametrically slower occurring on a timescale $t_\# \sim L$. Specifically, we can distinguish charge-sharp or charge-fuzzy behavior by the variance of the conserved charge $\mathcal{Q}$ in Eq. (2) over a single trajectory, averaged across trajectories and samples, i.e.,

$$[\delta\mathcal{Q}^2] = [\langle\mathcal{Q}^2\rangle_{\mathbf{m}} - \langle\mathcal{Q}\rangle_{\mathbf{m}}^2], \tag{4}$$

where the quantity in parentheses is the *quantum* number variance in a given trajectory. In the sharp phase, $[\delta\mathcal{Q}^2] = 0$, while in the fuzzy phase it remains nonzero at times of order $t \sim L$.

The dynamics of charge sharpening at small p can be qualitatively understood in terms of a simple classical model, in which one ignores the spatiotemporal correlations between measurements. One can then ask how many independent density measurements $\mathcal{N}_M$ are required to distinguish systems with N particles on L sites from those with $N-1$ particles on L sites, where $n \equiv N/L = \mathcal{O}(1)$. Assuming Gaussian density fluctuations (as in the $p = 0$ thermal state), we expect the N-particle and $(N-1)$-particle states to become distinguishable when $\mathcal{N}_M \sim L^2$ [61]. Since $\mathcal{N}_M = pLt$ in the circuits we consider, sharpening happens on a crossover timescale $t_\# \sim L/p$. For timescales $t \geq t_\#$, we expect that $[\delta\mathcal{Q}^2] \sim \exp(-t/t_\#)$. This follows, e.g., from using the central limit theorem to estimate the probability that an N-particle state will give an average density of $n \pm 1/L$ after pLt measurements. This simple model of the volume-law phase predicts that a crossover to charge sharpening should take place on a timescale $t_\# \sim L/p$, consistent with our numerical findings (see Secs. III and V), and parametrically faster than purification. Importantly, at any finite t/L, $[\delta\mathcal{Q}^2]$ remains nonzero in the fuzzy phase (albeit exponentially small for $t \gg t_\#$).

By contrast, for $p > p_\#$, charge sharpening happens on a timescale that is sublinear (logarithmic) in system size. In the limit $L \to \infty, t/L = \text{const}$, each trajectory has a definite charge. Thus there is a sharp phase transition at $p_\#$, for which $[\delta\mathcal{Q}^2]$ acts as an order parameter. Our numerical results also indicate that charges become devoid of quantum superposition in some regions of spacetime exhibiting locally minimal spacing of measurements (see Sec. V).

As with the entanglement transition, one can probe the charge-sharpening transition by coupling an ancilla to the circuit. One entangles the ancilla with the system such that each ancilla state is coupled to a system state with a different value of $\mathcal{Q}$. The system-ancilla entanglement vanishes when $\mathcal{Q}$ sharpens under the circuit dynamics.

3. Entanglement dynamics

We now turn to the dynamics of entanglement at times of order unity. Recall that, absent measurements, the Rényi entropies $S_n \sim \sqrt{t}$ for all $n > 1$ in random circuits with U(1) symmetric gates [52,54,62]. This diffusive entanglement dynamics appears to be a generic property of random circuits, so one might expect it to hold throughout the volume-law phase. If it held at the critical point, it would prevent the critical theory from being a conformal field theory (CFT). We now discuss why Rényi entropies in fact scale *ballistically* for any nonzero measurement probability, $p > 0$, allowing both the sharpening and entanglement transitions to obey relativistic $z = 1$ dynamic scaling.

First, we review the argument for diffusive scaling in the absence of measurements [52,54,62]. This phenomenon arises from rare fluctuations that leave a region empty (or maximally filled), as follows. Consider, for concreteness, the dynamics of the initial product state for the qubit $|\psi\rangle = \otimes_{i=1}^{L} |+_x\rangle_i$, where $|+_x\rangle = (1/\sqrt{2})(|0\rangle + |1\rangle)$. Suppose we are interested in the entanglement across a cut at $L/2$ at some later time t. We can divide the system into three regions: a central region of radius $\ell = \sqrt{Dt}$ centered at the entanglement cut, and regions to the left and right. Define

$$|\psi_{\text{dead}}\rangle = \bigotimes_{i=1}^{L/2-\ell} |+_x\rangle_i \bigotimes_{i=L/2-\ell+1}^{L/2+\ell} |0\rangle_i \bigotimes_{i=L/2+\ell+1}^{L} |+_x\rangle_i. \quad (5)$$

Initially, $|\langle\psi_{\text{dead}}|\psi\rangle| = 2^{-2\ell}$. After evolving for time t, $|(\langle\psi_{\text{dead}}|U_t^\dagger)(U_t|\psi\rangle)| = 2^{-2\ell}$ by unitarity. However, $U_t|\psi_{\text{dead}}\rangle$ is a product state with respect to the cut at $L/2$: by construction, t is not long enough for particles to have diffused to the entanglement cut, and unless there is a $|10\rangle$ or $|01\rangle$ configuration at the cut the gates acting across the cut cannot generate entanglement. The largest Schmidt coefficient of $U_t|\psi\rangle$ is its maximal overlap with *any* product state, so we can lower bound the largest Schmidt coefficient of $U_t|\psi\rangle$ as $2^{-2\ell} = 2^{-\sqrt{Dt}}$, and therefore $S_\infty \leq 2\ell \ln 2 \sim \sqrt{Dt}$. All Rényi entropies with $n > 1$ are dominated by this largest Schmidt coefficient and grow as $\sqrt{t}$. The von Neumann entropy S_1 is dominated instead by *typical* Schmidt coefficients: the number of these grows exponentially in t, but they are also exponentially small in t and are therefore subleading for $n > 1$.

We now address how this argument changes when $p > 0$. In a typical trajectory, on a timescale t, there are $p\ell t \sim pt^{3/2}$ measurements in the putative dead region near the entanglement cut, and about half the measurements observe a qubit to be in the charge state $|1\rangle$. There are rare circuits with few measurements near the cut, as well as rare histories in a typical circuit where all the measurements yield the same outcome $|0\rangle$. However, both are *at least* exponentially suppressed in ℓ and cannot dominate the trajectory-averaged entanglement (since *any* trajectory contributes at most $\sim t$ entanglement, and in any case these atypical trajectories have unusually slow entanglement growth). Therefore, to compute the trajectory-averaged Rényi entropies it suffices to consider trajectories with typical measurement locations and typical outcomes. In typical trajectories, one observes a $|1\rangle$ charge after $\mathcal{O}(1)$ measurements in the region near the cut, so the putative dead region survives only until a time $t \sim p^{-2/3}$. At longer times, the overlap of the wave function with dead regions is zero. We conclude that the trajectory-averaged Rényi entropies $[S_n]$ grow linearly in time whenever $p > 0$ [63]. We also note that the existence of diffusive hydrodynamic modes, which are a purely classical phenomena, does not affect the $z = 1$ dynamical scaling at the volume-to-area law entanglement transition at p_c. Our numerical estimates of the dynamic exponent in Sec. III are consistent with this result that $z = 1$ scaling applies and diffusive hydrodynamics decouples also at the charge-sharpening transition at $p_\#$.

III. NUMERICS ON QUBIT CHAINS

In this section, we present numerical results on a model of random U(1)-conserving gates acting on a chain of qubits (i.e., the $d = 1$ limit of the general model in Sec. II A). Specifically, in the basis of the adjacent qubits $\{|\downarrow\downarrow\rangle, |\uparrow\downarrow\rangle, |\downarrow\uparrow\rangle, |\uparrow\uparrow\rangle\}$ the 2-qubit gates at site i take the block diagonal form,

$$U_{i,i+1} = \begin{pmatrix} e^{i\phi_0} & & & \\ & U^1_{2\times 2} & & \\ & & & e^{i\phi_1} \end{pmatrix}, \quad (6)$$

where ϕ_1 and ϕ_0 are chosen at random from the interval $[0, 2\pi)$ and $U^1_{2\times 2}$ is a Haar-random 2×2 unitary matrix that can be parametrized by four angles,

$$U^1_{2\times 2}(\alpha, \phi, \psi, \chi) = e^{i\alpha} \begin{pmatrix} e^{i\psi}\cos\phi & e^{i\chi}\sin\phi \\ -e^{-i\chi}\sin\phi & e^{-i\psi}\cos\phi \end{pmatrix}, \quad (7)$$

where α, ψ, χ, and ϕ are chosen so that $U^1_{2\times 2}$ is uniformly sampled from U(2) [64]. In between layers of gates, projective measurements are performed: with a probability p, the qubit is projected onto $|\uparrow\rangle$ or $|\downarrow\rangle$ given by the Born rule. Utilizing the conservation law, we work in definite number sectors to reduce the memory load of the exact numerics.

The conservation law leads to different charge sectors defined by eigenspaces of $\mathcal{Q}$ in Eq. (2). We will typically focus on charge sectors near the central subspace ($\mathcal{Q} = L/2$).

A. Entanglement transition

We begin by locating the entanglement transition point p_c in this model. In order to probe the location of the critical point and the correlation length critical exponent, we study two quantities that have been identified as good measures of the transition: the tripartite mutual information [28] and an order parameter defined through the use of an ancilla [27] that is coupled to one charge-$\mathcal{Q}$ sector. In the following it is essential that we use an accurate estimate of p_c to be able to numerically disentangle it from the charge-sharpening transition at $p_\#$.

First, the tripartite mutual information for the Rényi index n is defined as

$$\begin{aligned}\mathcal{I}_{3,n}(A,B,C) \equiv\ & S_n(A) + S_n(B) + S_n(C) \\ & - S_n(A\cup B) - S_n(A\cup C) - S_n(B\cup C) \\ & + S_n(A\cup B\cup C), \end{aligned} \quad (8)$$

where we have chosen regions A, B, and C to be adjacent regions of size $L/4$ and $S_n(A)$ is the Rényi entropy defined in Eq. (1). For $\mathcal{I}_{3,n}$ at late times ($t = 4L$) we apply the finite size scaling hypothesis $\mathcal{I}_{3,n} \sim f[L^{1/\nu}(p - p_c)]$, to locate the critical point, where $f(x)$ is a scaling function and ν is the correlation length exponent. The data for $n = 1$ are shown in Fig. 2(a) where we find the data collapse with the minimum χ^2 for the choice of $p_c = 0.105(3)$ and $\nu = 1.32(6)$. The error bars are estimated by a region in

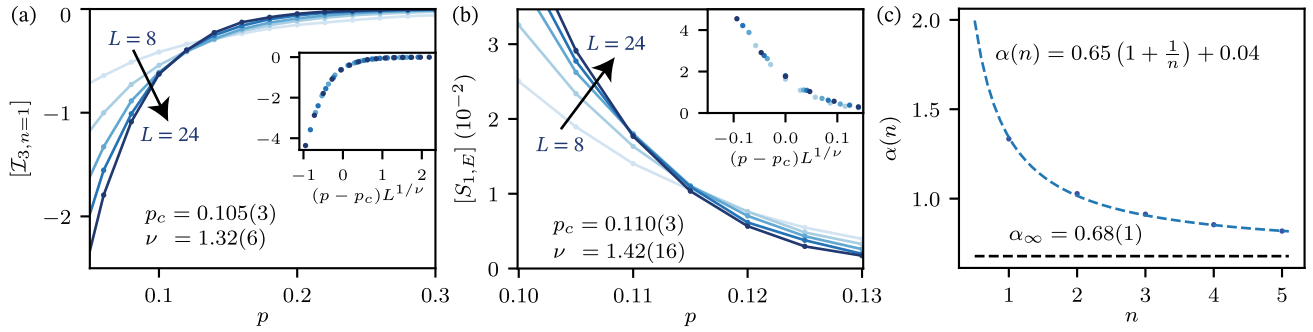

FIG. 2. Entanglement transition in qubit chains. (a) Data and collapse of the tripartite mutual information $\mathcal{I}_{3,n=1}$ used to determine the critical point of the entanglement transition, $p_c = 0.105(3)$, and the correlation length exponent, $\nu = 1.32(6)$. The error bars in p_c and ν are estimated using the region in parameter space near the minimum such that $\chi^2 < 1.3\chi^2_{\text{min}}$ [28]; see Fig. 5. (b) Data and collapse of the entanglement transition order parameter $[S_{1,E}]$ used as an alternative method to determine the critical point of the entanglement transition, $p_c = 0.110(3)$, and the correlation length exponent, $\nu = 1.42(16)$. The critical point and the exponent for $[S_{1,E}]$ are estimated with a finite size scaling analysis as explained in Appendix D. (c) At the critical point, the bipartite entanglement entropy shows logarithmic scaling with the system size. The coefficient of the logarithm has strong Rényi index dependence that can be described by a functional form $\alpha(n) = 0.65(1)[1 + (1/n)] + 0.04(1)$. The error bars in $\alpha(n)$ are obtained from the standard deviation of the fit parameters in $\alpha(n) \sim a[1 + (1/n)] + b$ while the error in the data points themselves take into account the standard deviation of the fit parameters in $S_n(p_c, L) \sim \alpha(n) \ln L$ and the error in p_c. This closely resembles the standard result for the ground state of a CFT, but has an offset slightly larger than zero. Error bars on the data points are obtained from the error on the mean by computing the standard deviation.

parameter space near the minimum such that $\chi^2 < 1.3\chi^2_{\text{min}}$ [28]; see Fig. 5. A similar analysis can be performed for the other Rényi entropies, and the resulting values of p_c and ν are similar for all $n \geq 1$ investigated; we find $p_c = 0.103(4), 0.12(2), 0.12(1)$ and $\nu = 1.37(8), 1.47(3), 1.5(2)$ for $n = 2, 5, \infty$, respectively.

At the critical point, the bipartite entanglement entropy shows a logarithmic dependence on the system size and the coefficient of the logarithmic divergence shows strong Rényi index dependence [Fig. 2(c)]. This behavior can be described by

$$S_n(p_c, L) \sim \alpha(n) \ln L,$$
$$\alpha(n) = 0.65(1)\left(1 + \frac{1}{n}\right) + 0.04(1). \tag{9}$$

Apart from the small offset, this Rényi index dependence matches the result one expects for the ground state of a CFT [4], $\alpha_{\text{CFT}}(n) = \frac{c}{6}[1 + (1/n)]$. The coefficients in Eq. (9) clearly differ from those at the measurement-induced transition without a conservation law [28].

As an alternative way of locating the entanglement transition, we also study the "order parameter" [27]. In order to have the ancilla couple to the system within a particular global charge sector, we consider the qubits at two adjacent sites i and $i + 1$ to be in the entangled state with an ancilla: $|\Psi_0\rangle = (1/\sqrt{2})(|\uparrow\downarrow\rangle|1\rangle + |\downarrow\uparrow\rangle|0\rangle)$, where the ancilla has orthogonal basis states $|1\rangle$ or $|0\rangle$. We then evolve the system in time $t = 2L$ without measurements in order to create a state $|\Psi\rangle = (1/\sqrt{2})(|\psi_1\rangle|1\rangle + |\psi_0\rangle|0\rangle)$, where $|\psi_{0,1}\rangle$ are orthogonal and in the same charge sector. We then run the circuit with measurements for an additional time $2L$ and compute the von Neumann entropy of the ancilla, which we denote as $S_{1,E}$ (as it probes the entanglement transition).

The results for the von Neumann entanglement entropy of the ancilla $S_{1,E}$ are shown in Fig. 2(b), and are consistent with $\mathcal{I}_{3,n}$ data: From the scaling ansatz $S_{1,E} \sim f_E((p - p_c)L^{1/\nu})$, where $f_E(x)$ is a universal scaling function, we obtain $p_c = 0.110(3)$ and $\nu = 1.4(2)$ in good agreement with $\mathcal{I}_3$.

Summarizing these results, the entanglement transition in U(1) symmetric circuits has a critical exponent ν that is consistent with the value for Haar-random circuits with no symmetries, although the nonuniversal p_c has drifted down from the Haar value $p_c^{\text{Haar}} \approx 0.17$ (as one might expect since each gate cannot generate as much entanglement). At $p = p_c$ we extract the dynamical exponent of the entanglement transition using the scaling ansatz $[S_{1,E}] \sim g_E(t/L^z)$, which shows a good quality as seen in Fig. 4 for $z = 1$ and $g_E(x)$ some universal scaling function. Again, this result is consistent with the nonconserving case. While we have focused on $\mathcal{Q} = L/2$, we have checked that for the largest system sizes considered p_c is only very weakly affected for $\mathcal{Q} = L/2 - 1$ (not shown).

B. Charge-sharpening transition

We now turn to estimating $p_\#$ in two ways: the charge variance of a state and the entropy of an ancilla entangled with two different number sectors.

First, we compute the variance of the total charge [Eqs. (2) and (4)]. For a trajectory that lies in a

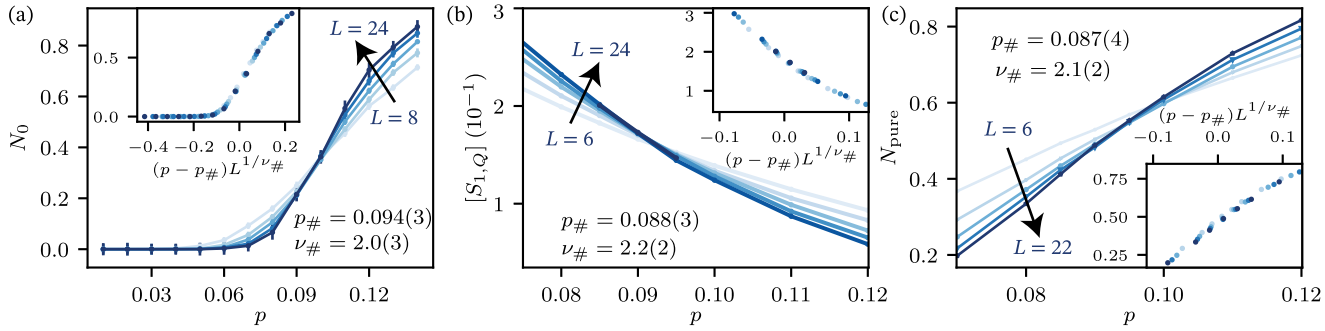

FIG. 3. Charge-sharpening transition in qubit chains. (a) Data and collapse of N_0, the fraction of trajectories with $\delta\mathcal{Q}^2 < \epsilon$ used to determine the critical point of the charge-sharpening transition, $p_\# = 0.094(3)$, and correlation length exponent, $\nu_\# = 2.0(3)$. The value of $\epsilon = 10^{-2}$ is chosen such that it maximizes the quality of collapse at $t/L = 4$. The error bars in $p_\#$ and $\nu_\#$ are estimated using the region in parameter space near the minimum such that $\chi^2 < 1.3\chi^2_{\text{min}}$ [28]; see Fig. 5. (b) Data and collapse of the charge-sharpening transition order parameter $[S_{1,Q}]$ used as an alternative method to determine the critical point of the sharpening transition, $p_\# = 0.088(3)$, and the correlation length exponent, $\nu_\# = 2.15(15)$. (c) Data and collapse of the fraction of trajectories where the ancilla qubit is purified N_{pure} at the charge-sharpening transition. The transition point $p_\# = 0.087(4)$ and the correlation length exponent $\nu_\# = 2.1(2)$ are consistent with the ancilla probe. The critical point and the exponent obtained from $[S_{1,Q}]$ and N_{pure} are estimated with a finite size scaling analysis as explained in Appendix D. Error bars on the data points are obtained from the error on the mean by computing the standard deviation.

well-defined charge sector, $\delta\mathcal{Q}^2 = 0$, otherwise $\delta\mathcal{Q}^2 \neq 0$. Therefore, we start with a pure initial state that is spread out over all of the different $\mathcal{Q}$ sectors, $|\psi_0\rangle = \otimes_{i=1}^{L} (1/\sqrt{2})(|\uparrow\rangle_i + |\downarrow\rangle_i)$, and run the conserving hybrid dynamics to late times to determine if the system has sharpened into a single charge sector for some measurement probability $0 \leq p_\# \leq p_c$, where $p_c \approx 0.11$ is the critical point of the entanglement transition. In this situation, the critical point of the charge sector transition can be determined by studying the probability, $P(\delta\mathcal{Q}^2 = 0)$. [Recall that $\delta\mathcal{Q}^2$ is a quantum uncertainty that is a property of each trajectory; the probability distribution $P(\delta\mathcal{Q}^2)$ is over trajectories and circuits, where each trajectory is weighted by its Born probability.] For large systems, $P(\delta\mathcal{Q}^2 = 0) \to 0$ when the system is distributed over multiple sectors while $P(\delta\mathcal{Q}^2 = 0) \to 1$ when the system has been constrained to a single sector. In Fig. 3(a), the fraction N_0 of trajectories having a variance $x = \delta\mathcal{Q}^2 \leq s$ (with $s = 10^{-2}$) is shown for various system sizes and measurement probabilities. The critical point can be identified by the crossing near $p = 0.1$. Performing a finite size scaling analysis, we find the data for different system sizes collapse onto a universal curve for the critical point $p_\# = 0.094(3)$ and correlation length exponent $\nu_\# = 2.0(3)$.

Lastly, we consider an ancilla coupled to two different charge sectors; in particular, we take $|\Psi\rangle = |\psi_\mathcal{Q}\rangle|0\rangle + |\psi_{\mathcal{Q}-1}\rangle|1\rangle$ where $|\psi_\mathcal{Q}\rangle$ represents states within the charge sector $\mathcal{Q}$ (while $|1\rangle$ and $|0\rangle$ are states of the ancilla as before). Since there is no unitary that mixes these sectors, we can say definitively that the reduced density matrix has the form

$$\rho_{\text{anc}} = \begin{pmatrix} |\langle\psi_\mathcal{Q}(t)|\psi_\mathcal{Q}(t)\rangle|^2 & 0 \\ 0 & |\langle\psi_{\mathcal{Q}-1}(t)|\psi_{\mathcal{Q}-1}(t)\rangle|^2 \end{pmatrix}. \quad (10)$$

This formulation is convenient for the numerical algorithm we have developed that conserves charge since if the ancilla were just considered an extra qubit, $|\Psi\rangle$ would be in the conserving sector M for $L+1$ qubits. Doing this, we compute the von Neumann entanglement entropy of the ancilla qubit that we denote as $S_{1,\mathcal{Q}}$, that is shown in Fig. 3(b). Based on the crossing in the data and the ansatz $S_{1,\mathcal{Q}} \sim g_\mathcal{Q}((p - p_\#)L^{1/\nu_\#})$, we obtain $p_\# = 0.088(3)$ and $\nu_\# = 2.2(2)$, which matches the $p_\#$ and $\nu_\#$ found by $P(\delta\mathcal{Q}^2 = 0)$. In addition, we extract the charge-sharpening transition from the probability that the ancilla has fully disentangled from the circuit by computing the fraction of trajectories N_{pure} that have fully purified the ancilla [Fig. 3(c)]. From the crossing of N_{pure}, we find a third consistent estimate of $p_\#$ and $\nu_\#$. Thus, we have identified the charge-sharpening transition across all sectors of $\mathcal{Q}$ with the transition in $S_{1,\mathcal{Q}}$ across $\mathcal{Q} = L/2, L/2 - 1$. The dynamical exponent of the charge-sharpening transition is also $z = 1$, as $[S_{1,\mathcal{Q}}] \sim g_\mathcal{Q}(t/L)$ at criticality (Fig. 4).

The two critical points we have identified in this model at $p_\#$ and p_c are at least ~3.5 error bars from each other, providing evidence that a charge-sharpening transition occurs *before* full purification. This is further exemplified by the estimated confidence intervals for the two transitions for the various probes we have considered as shown in Fig. 5. Moreover, the correlation length exponent for charge-sharpening quantities is distinct from that of the entanglement purification transition, further suggesting that

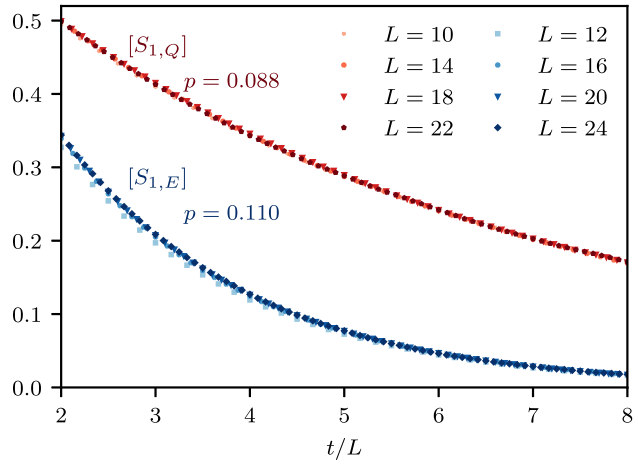

FIG. 4. Dynamical exponent. Plot of the rescaled time dependence of the ancilla-circuit entanglement entropy for the entanglement transition at $p = p_c \approx 0.11$ (blue curve) and the charge-sharpening transition at $p = p_\# \approx 0.088$ (red curve). The finite size collapse indicates a dynamical exponent $z = 1$ for both transitions.

these represent distinct critical points with different universality classes.

We note, however, that the close proximity of the putative two transitions makes them challenging to cleanly separate numerically in small-scale systems, and acknowledge that this data could in principle be accounted for by large, systematic finite size errors in the critical exponents

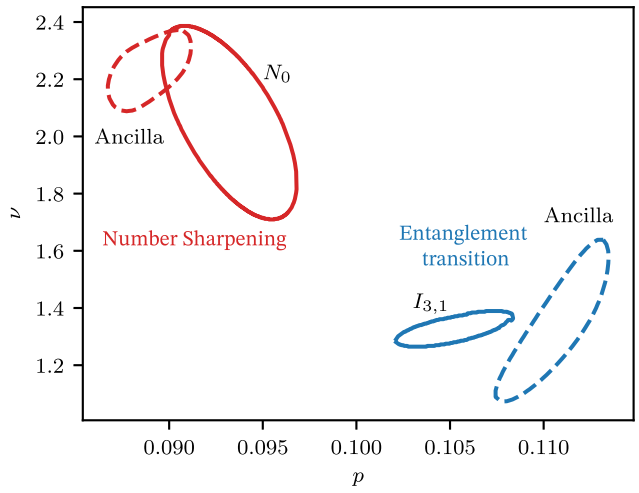

FIG. 5. Two transitions. Plot of the 68% confidence interval of the critical point p and the correlation length exponent ν for both the entanglement and charge transitions. The mutual information $I_{3,1}$ (solid blue circle) and the ancilla probe (dashed blue circle) are for the entanglement transition, while the fraction of trajectories N_0 (solid red circle) and the ancilla probe (dashed red circle) are for the charge-sharpening phase transition. The two transitions appear to be different with statistical significance, although we cannot exclude systematic finite size effects that would change this conclusion in the thermodynamic limit.

that affected the charge and entanglement properties differently [65]. In the following sections, we see that for the model with large-d qudits, the location of the two transitions become clearly distinct.

IV. STATISTICAL MECHANICS MODEL

In this section, we show that in the $d \to \infty$ limit, the calculation of entanglement in monitored U(1) circuits can be mapped exactly onto a classical statistical model defined on a square lattice. In this limit, the contributions to the entanglement entropy from the qubit with conserving dynamics and the qudit decouple. The resulting qubit contribution can then be obtained from a constrained symmetric exclusion process.

Our main goal is to compute averaged Rényi entropies $[S_n]$. The Rényi entropies of a spatial subregion A for a fixed quantum trajectoryare given by

$$S_n(A, \mathbf{m}) = \frac{-1}{n-1}[\ln \mathrm{Tr}(\rho_{\mathbf{m}}^{\otimes n} T_{n,A}) - \ln \mathrm{Tr}\rho_{\mathbf{m}}^{\otimes n}], \tag{11}$$

where $\rho_{\mathbf{m}} = |\psi_{\mathbf{m}}(t)\rangle\langle\psi_{\mathbf{m}}(t)|$, $|\psi_{\mathbf{m}}(t)\rangle = K_{\mathbf{m}}|\psi_0\rangle$ is the state ("trajectory") of the system after evolution by time t for a measurement history $\mathbf{m}$, and $T_{n,A}$ is a SWAP operator permuting the n copies of the input state in the entanglement region A:

$$T_{n,A} = \prod_i |s_{\sigma_i(1)} s_{\sigma_i(2)} \ldots s_{\sigma_i(n)}\rangle\langle s_1 s_2 \ldots s_n|,$$
$$\sigma_i = \begin{cases} \text{identity} = e & i \notin A \\ (12\ldots n) & i \in A, \end{cases} \tag{12}$$

where the index i runs over all physical sites, $|s_i\rangle$ are members of the on-site Hilbert space, σ_i is an element of the permutation group $\mathcal{S}_n$, and $(12\ldots n)$ denotes a cyclic permutation of the n copies of ρ. The key technical difficulty in this problem is to perform the average over gates, measurement locations, and outcomes, and to normalize the state after the projective measurements since entanglement is intrinsically nonlinear in the density matrix. To bypass this problem, we follow Refs. [19,20] (see also Refs. [66,67] in the context of random tensor networks) and introduce k replica copies of the system. The average Rényi entropy S_n is then written as

$$[S_n] = \lim_{k\to 0} \frac{-1}{k(n-1)} \sum_{\mathbf{m}} [Z_A(\mathbf{m}) - Z_\varnothing(\mathbf{m})], \tag{13}$$

where

$$Z_A(\mathbf{m}) = \mathbb{E}_U\{\mathrm{Tr}[(K_{\mathbf{m}}|\psi_0\rangle\langle\psi_0|K_{\mathbf{m}}^\dagger)^{\otimes nk+1} T_{n,A}^{\otimes k}]\},$$
$$Z_\varnothing(\mathbf{m}) = \mathbb{E}_U\{\mathrm{Tr}[(K_{\mathbf{m}}|\psi_0\rangle\langle\psi_0|K_{\mathbf{m}}^\dagger)^{\otimes nk+1}]\}, \tag{14}$$

with $T_{n,A}$ defined in Eq. (12), and $|\psi_0\rangle$ is the quantum state of the system at $t = 0$. As the notation suggests, $Z_{A,\varnothing}$ will

correspond to the partition function of an effective statistical model, where Z_A and $Z_\varnothing$ only differ with respect to the boundary condition at the top boundary region A (see Fig. 11 in Appendix A). We denote the total number of replicas as $Q = nk + 1$ in the subsequent discussion. The additional replica is due to the Born probability factor, which ensures quantum trajectories are weighted appropriately [20]. Also note that since the original nonlinear quantity has been converted to a linear quantity defined on Q copies, we are free to do various averages in any order we want.

The rest of this section is organized as follows. We start by giving a very brief overview of the statistical model for random monitored circuits without any symmetries, following Refs. [19,20], before moving on to summarize the result for the U(1) symmetric system. We include a detailed and technical derivation of the above model in Appendix A. This technical section can be skipped without breaking any continuity.

A. Statistical model for systems without symmetry

We briefly review the mapping for random monitored circuits without symmetries to a statistical model [19,20]. We focus on the details required for our subsequent discussion, in particular on the large dimension limit $d \to \infty$. To calculate Eq. (14) we need to average over Q copies of the circuit over Haar gates and measurement outcomes (but *not* over measurement locations). Since the random Haar gates are drawn independently, we can individually average Q copies of each gate. The combinatorial results of the averaging can be captured as a partition function that can be computed as follows: each unitary gate in the circuit is replaced by a vertex associated with a pair of permutation "spins" $\sigma_a, \bar{\sigma}_a$, each belonging to the permutation group $\mathcal{S}_Q$. In the $d \to \infty$ limit, these spins become locked together in a single $\mathcal{S}_Q$ degree of freedom, σ_a. Vertices from adjacent gates, i.e., those which share an input or output qubit, are connected by links. The weight associated with a vertex in the partition function is given by $V_a = 1/d^{2Q}$. The weight of the links connecting vertices with elements $\sigma_{a,b}$ is given by

$$W_{ab}[\sigma_b^{-1}\sigma_a] = \begin{cases} d^{|\sigma_b^{-1}\sigma_a|} & \text{if link } (ab) \text{ is not measured} \\ d & \text{if link } (ab) \text{ is measured,} \end{cases} \tag{15}$$

where $|\sigma_b^{-1}\sigma_a|$ is equal to the number of cycles in the cycle decomposition of $\sigma_a^{-1}\sigma_b = C_1 \ldots C_{|\sigma_b^{-1}\sigma_a|}$. Note that the above weights are symmetric under left and right multiplication by elements of $\mathcal{S}_Q$.

We see that in this $d \to \infty$ limit, spins (permutations) connected by unmeasured links are forced to be the same, whereas spins on measured links are effectively decoupled; i.e., measurements "break" the links connecting permutation spins, diluting the lattice. This naturally yields a picture of the purification transition in terms of *classical percolation* of clusters of aligned permutation "spins" [14,19,20], though of course this simple percolation picture is special to $d \to \infty$: $1/d$ fluctuations are a relevant perturbation to the percolation critical point such that finite d transitions are described by a distinct universality class from percolation [20,22].

As we saw in Eq. (13), the calculation of S_n requires taking the difference between two partition functions of the model described above but with different boundary condition (see Fig. 11); in the replica limit, this difference in partition functions becomes equivalent to a difference in free energies $F_{A,\varnothing} = -\log Z_{A,\varnothing}$ (since the partition functions approach unity in the replica limit). The boundary condition for the calculation of Z_A forces a different boundary condition in region A, and thus introduces a domain wall (DW) near the top boundary. In the limit $d \to \infty$, the DW is forced to follow a minimal cut, defined as a path cutting a minimum number of unmeasured links (assumed to be unique for simplicity [68]). This can be seen as follows: because of the boundary condition in $Z_\varnothing$, all vertex elements in $Z_\varnothing$ are equal [69], and $Z_\varnothing = d^{(1-Q)N_m}$, where N_m is the number of measured sites. Z_A would be the same as $Z_\varnothing$ except for the fact that due to the DW some links contribute different weights to Z_A. More precisely, we have $Z_A = d^{(k+1-Q)\ell_{\mathrm{DW}}} Z_\varnothing$, where $\ell_{\mathrm{DW}} = \ell_{\mathrm{DW}}(\mathbf{X})$ is equal to the number of unmeasured links that the DW crosses. Since $k + 1 - Q = (1-n)k < 0$ for $n > 1$, the DW will follow the path that minimizes ℓ_{DW} [70]. Using the expression of $Z_{A,\varnothing}$ in Eq. (13) and taking the replica limit $k \to 0$, we find $S_n = \ell_{\mathrm{DW}}(\mathbf{X}) \ln d$, which is valid for each configuration of measurement locations. Averaging over measurement locations, we have

$$[S_n] = [\mathbb{E}_{\mathbf{X}} \ell_{\mathrm{DW}}(\mathbf{X})] \ln d, \tag{16}$$

where $\mathbf{X}$ denotes a configuration of measurement locations (measurement outcomes and Haar gates have been averaged over to get the statistical model). In the language of the statistical model, $\mathbf{X}$ denotes a percolation configuration. and ℓ_{DW} is the length of the minimal cut from one end of the subsystem A to the other end.

In the $d \to \infty$ limit, Eq. (16) is valid for any measurement probability p [71]. For $p = 0$, there are no measured links and, hence, $\ell_{\mathrm{DW}} = |A|$, where $|A|$ is the length of subsystem A. In fact, ℓ_{DW} undergoes a percolation transition at $p_c = 1/2$, where ℓ_{DW} is extensive in $|A|$ for $p < 1/2$, and becomes $\mathcal{O}(1)$ for $p > 1/2$ [14].

B. Statistical model with U(1) qubits—Summary

Here we provide a concise summary of the statistical model in the case of U(1) circuits, deferring the technical details to Appendix A.

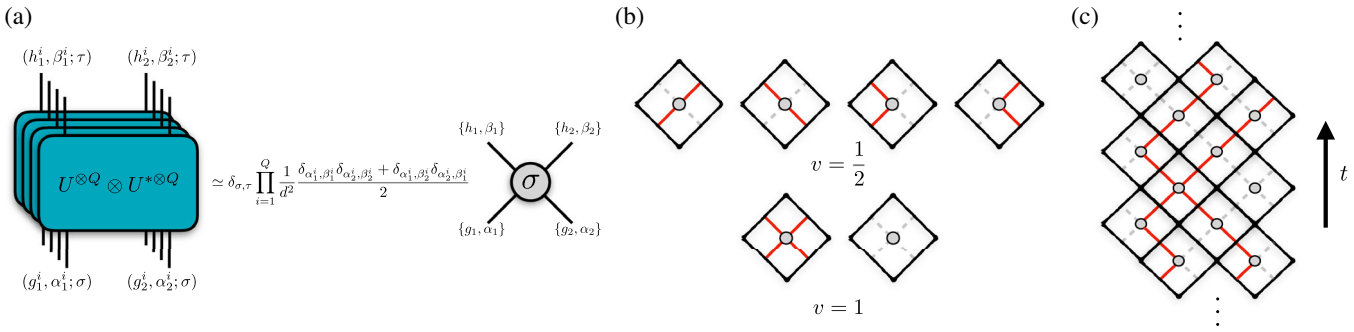

FIG. 6. Statistical mechanics model. (a) The average of $\mathcal{U} = U^{\otimes Q} \otimes U^{*\otimes Q}$ over Haar gates is nonzero if and only if the conjugate (bra) replicas are permutations of the nonconjugate (ket) replicas. Hence we can conveniently write each leg in the circuit as a set of Q copies of nonconjugate states combined with a permutation group element [see Eq. (A1)]. In the large-d limit, the permutation group elements for ingoing and outgoing legs become locked together in a single permutation, and the corresponding permutation group element σ can be associated with a vertex (one per gate), while the charge states live on links. The U(1) charges α, β are constrained by charge conservation. (b) The charge dynamics in each replica are given by an effective 6-vertex model with weights v, corresponding to a symmetric exclusion process constrained by the measurements and entanglement cut. (c) Example of charge configuration.

Introducing a U(1) qubit on top of each qudit modifies the above model by introducing an additional degree of freedom (per replica) α_{ij} defined on links, which can take value 0 or 1 and correspond to the charge of the U(1) qubits. The weight of each vertex is modified according to the input and output U(1) charges as follows,

$$\begin{aligned}
&(1,1) \to (1,1),\\
&(0,0) \to (0,0),\\
&(1,0) \to \frac{1}{2}[(1,0)+(0,1)],\\
&(0,1) \to \frac{1}{2}[(1,0)+(0,1)],
\end{aligned} \tag{17}$$

where the left-hand side denotes the two input charges and the right-hand side denotes output charges. The constants before the output spins are the contribution to the vertex weights. For all other configurations of charges, the weight is equal to 0, thereby enforcing charge conservation. These rules can also be seen as a special case of a 6-vertex model where the states 0,1 denote two species of links and the weight of the vertex depends on the configuration of the links around the vertex; see Fig. 6. Alternatively, those weights can be interpreted as describing hard-core random walkers (symmetric exclusion process), where each state "1" corresponds to a walker (solid link), with the number of walkers being conserved as a function of time (vertical direction in the statistical mechanics model).

We cannot directly average over the measurement outcomes of the U(1) qubits due to the nonlocal nature of the vertex weights. Hence, we only write a statistical model for a given set of measurement locations $\mathbf{X}$ and outcomes $\mathcal{M}(\mathbf{X})$ for the U(1) qubits; we collectively denote this set by $\mathbf{m}$, as above. The charges in the statistical model at broken links of the percolation sample are pinned by the measurement outcome of the qubit on that link. In other words, for a given configuration $\mathbf{m}$, all measured links (broken links in the percolation cluster) carry a fixed value of the local charge 0 or 1 determined by the measurement outcome of the qubit, which is fixed in $\mathbf{m}$.

The statistical model is then given by

$$Z(\mathbf{m}) = \sum_{\{\alpha\}} \prod_{i \in \text{vertices}} V_i(\{\alpha\}), \tag{18}$$

where the sum over $\{\alpha\}$ denotes the sum over the set of charges α on all links, V_i is the 6-vertex model weight corresponding to the rules (17), and $\mathbf{m}$ represents a percolation configuration combined with a set of values of pinned charges on broken links, corresponding to the measurement outcomes of the qubits on those links. This statistical model has a straightforward physical interpretation: it counts histories of the charge degrees of freedom compatible with a given set of measurement locations and measurement outcomes.

To calculate $S_n(\mathbf{m})$, we first need to find the minimal cut in the percolation configuration. Recall that ℓ_{DW} is the number of unbroken links (not measured) along the cut. There are $2^{\ell_{\text{DW}}}$ different charge configurations along the cut; we denote this set of different configurations by $\{\beta_{\text{DW}}\}$. From the partition function (18), one can straightforwardly compute the probability of finding configuration β_{DW} along the minimal cut. We denote this $p_{\beta_{\text{DW}}}$. Taking the replica limit exactly (see Appendix A), we find that the Rényi entropy is given by

$$S_n(\mathbf{m}) = \frac{-1}{n-1} \ln \left(\sum_{\{\beta_{\text{DW}}\}} p_{\beta_{\text{DW}}}^n \right) + \ell_{\text{DW}} \ln d. \tag{19}$$

The entropy S_n averaged over all trajectories is then given by

$$[S_n] = \sum_{\mathbf{m}} Z(\mathbf{m}) S_n(\mathbf{m}), \tag{20}$$

where $Z(\mathbf{m})$ in Eq. (18) can be interpreted as some effective Born probability for observing the trajectory $\mathbf{m}$, where unitary gates have been averaged over. In particular, note that $\sum_{\mathbf{m}} Z(\mathbf{m}) = \mathbb{E}_{\mathbf{X}} \sum_{\{\mathcal{M}(\mathbf{X})\}} Z(\mathbf{m}) = 1$.

Note that the second term in Eq. (19) is the entropy of a pure qudit system. We thus interpret the first term as coming from the qubit sector and treat it as the qubits' contribution to the entanglement entropy. This first term also has an appealing physical interpretation as the classical Rényi entropy of qubit configurations along the minimal cut. This is a special feature of the $d \to \infty$ limit. From now on, we will use S_n^T to denote total entropy of the qubits and qudits in Eq. (19), S_n^d for the contribution to the entropy from the qudit sector alone, and $S_n = S_n^T - S_n^d$ which is equal to the first term in Eq. (19).

While this expression can, in principle, be computed using Monte Carlo sampling with *no sign problem*, for the one-dimensional systems considered here, we find it more convenient to use a disordered transfer matrix to evolve the initial state up to some time t. Specifically, we fix $\mathbf{m}$ by randomly generating a percolation configuration, and use the vertex rules described in Eq. (17) to evolve the system in time. At each broken link (measured qubit) encountered in the evolution, we choose the outcome of the measurement (and hence the fixed value of the charge degree of freedom on that link) with probability equal to the Born probability. This is equivalent to a Monte Carlo sampling for the probability distribution given by $Z(\mathbf{m})$ in Eq. (18). Many samples are generated, and for each sample we calculate the probability distribution $\{p_{\beta_{\mathrm{DW}}}\}$. Any physical quantity is then calculated as $[O] = [\sum_{i=1}^{N_s} O(\mathbf{m})/N_s]$, where N_s is the number of samples generated.

We remark that, in addition to the direct simulation of the transfer matrix techniques we employ in this work, it could also be interesting to investigate further the scaling of the transition using tensor network techniques applied to the transfer matrix of the constrained 6-vertex model [72].

V. NUMERICAL RESULTS FROM THE STATISTICAL MECHANICS MODEL

In this section, we present numerical results for the U(1) statistical mechanics of constrained symmetric exclusion process described in the previous section, valid in the $d \to \infty$ limit. Unless otherwise stated, we focus on the contribution of the qubit to entanglement, and ignore the qudit contribution $\ell_{\mathrm{DW}} \ln d$ which is entirely given by classical percolation physics. We first present late time ($t \sim L$) entanglement data, and present evidence for the existence of the charge-sharpening transition occurring for $p_\# = 0.315 \pm 0.01 < p_c = \frac{1}{2}$. We also analyze the time dependence of the Rényi entropies, and show that they all grow linearly in time for any $p > 0$, in sharp contrast with the $p = 0$ behavior.

A. Charge-sharpening transition

In the statistical model, the total entanglement entropy of the subsystem A, S_n^T, depends on the minimal cut which undergoes a percolation transition at $p_c = \frac{1}{2}$; for $p < p_c$, the length of the minimal cut scales with L_A, while for $p > p_c$ the measurement locations percolate and ℓ_{DW} becomes $\mathcal{O}(1)$. Clearly the total entanglement entropy follows the area law for $p > p_c$, and is extensive (and dominated by the qudit contribution) for $p < p_c$. As discussed below Eq. (20), S_n^T is given by the sum of two contributions from the qudit and qubit sectors, respectively. In what follows, we focus on the qubit contribution $S_n = S_n^T - S_n^d$, and argue that this quantity undergoes an entanglement transition from volume law to area law for $p = p_\#$. We will show that this entanglement transition from the qubit sector coincides with a charge-sharpening transition, which can also be diagnosed in a scalable way using a local ancilla probe, as in Sec. III.

1. Entanglement transition in the qubit sector

In this section, we look at the Rényi entropies S_n at long times $t > 4L$ as a function of p. We consider the qubit initial state $|\psi_0\rangle = (|0\rangle + |1\rangle/\sqrt{2})^{\otimes L}$. To study the behavior of S_n for $p > 0$, we numerically run the statistical model (19) and calculate the half system S_n by averaging S_n over various time steps in the interval of 4 for $t > 4L$. We present results for the S_1 in Fig. 7.

In analogy with the nonsymmetric measurement transition [14,23], we use the following scaling ansatz for S_n:

$$[S_n] - S_n^c = f(L/\xi), \tag{21}$$

where $\xi \sim (p - p_\#)^{-\nu_\#}$, and $S_n^c = [S_n(p_\#)] \sim \alpha_n \ln L$. Using both the entanglement entropy scaling and tripartite mutual information as in Sec. III, we find that the qubit contribution shows an entanglement transition from volume law to area law at a critical value $p_\#$ less than $p_c = 1/2$. Finite size collapses are compatible with $p_\# = 0.3 \pm 0.02$ and $\nu_\# = 1.3 \pm 0.2$. We emphasize that this entanglement transition occurs *inside* the entangling phase of the total system (the qudit contribution obeys a volume-law scaling in this regime), and occurs only as a subleading contribution to the total entanglement entropy.

From the point of view of the statistical mechanics model, this transition is especially surprising, as it indicates that the entropy (19) of the charge degrees of freedom along the minimal cut does not scale with its length for $p > p_\#$. Instead, our numerical results indicate that measurements are enough to constrain most charges along the cut, so the

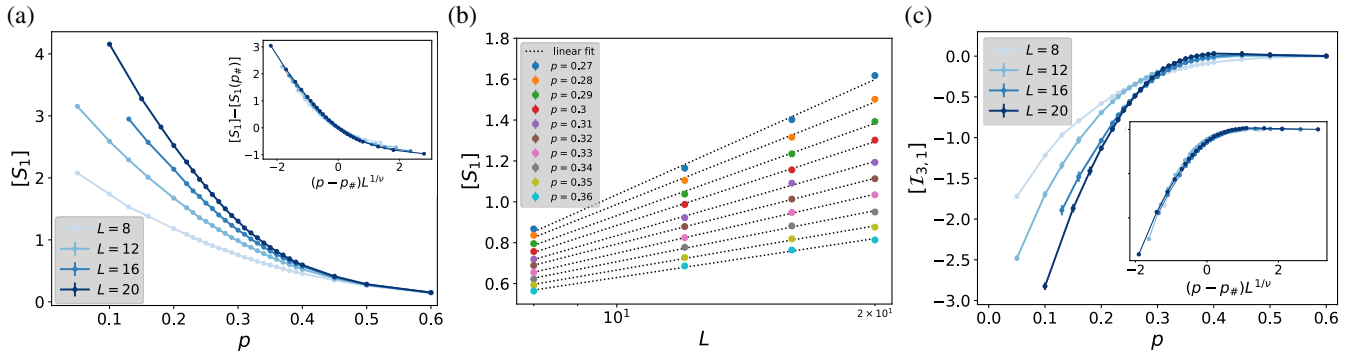

FIG. 7. Entanglement transition in the statistical model qubit contribution. (a) Plot of the qubit entanglement entropy S_1 versus p. The inset shows the finite size collapse using the ansatz discussed in the main text, with $\nu \sim 1.3$ and $p_\# \approx 0.29$. (b) Plot of S_1 versus L near the critical point. We find that at the critical point S_1 grows logarithmically with L. (c) Tripartite mutual information $\mathcal{I}_{3,1}$ versus p, showing a crossing around $p_\# \approx 0.29$. The inset shows the finite size collapse using the same correlation length exponent as in (a). Error bars on the data points are obtained from the error on the mean by computing the standard deviation.

charges are almost completely "frozen" [73] by the measurements near the minimal cut.

2. Charge-sharpening transition

Following Sec. III we probe charge sharpening by following the dynamics of the single-trajectory charge variance $\delta\mathcal{Q}^2_{\mathbf{m}}$ starting from an initial pure state that is a superposition over charge sectors. We first discuss the average of this quantity over all trajectories. We compute this quantity using the statistical model and plot $[\delta\mathcal{Q}^2]$ as a function p in Fig. 8(a). We see that for $p \gtrsim p_\# \approx 0.3$, which is the threshold of the area-law phase in the qubit sector, $[\delta\mathcal{Q}^2]/L$ goes to zero exponentially as a function of time in a way that is independent of L. This implies that the timescale $t_\#$ for charge sharpening for $p > p_\#$ (defined as the time it takes for the charge variance to reach a given small value ϵ) scales logarithmically with system size. In contrast, for $p < p_\#$, this charge-sharpening time scales as $t_\# \sim L$ (see Appendix C 2). Fixing $t = 2L$, $[\delta\mathcal{Q}^2]$ behaves as an order parameter for the charge-sharpening transition, coinciding with the entanglement transition in the qubit sector described in the previous section. We observe the same behavior in the bipartite charge variance.

To extract $p_\#$ it is useful to analyze a quantity that has a discontinuity at the transition. To this end, we consider N_0, the fraction of trajectories with $\delta\mathcal{Q}^2_{\mathbf{m}} < \epsilon$ for a given threshold ϵ, as in Sec. III. We check that the results do not depend on ϵ for small enough values. We plot this quantity in Fig. 8(b) and find a crossing around $p_\# = 0.31$. Note that for all L, we chose ϵ to be small enough so that N_0 counts only configurations where the charge is essentially perfectly sharp to numerical accuracy. Defined in this way, N_0 approaches 0 in the fuzzy phase, while it goes to 1 in the sharp phase. If we increase the threshold ϵ, instead, we find that N_0 behaves more like an order parameter, being fixed to $N_0 = 1$ in the sharp phase and continuously decreasing in the fuzzy phase. It is possible that the above transition in terms of the fraction of *exactly sharp* trajectories N_0 may be special to the case of perfectly projective measurements, as any slight weakening of the measurements would allow some nonzero quantum fluctuations of charge to persist in a finite spacetime volume. Nevertheless, the transition in N_0 provides an upper bound for the "true" sharpening transition, and can, for example, establish whether the true sharpening transition resides within the volume-law phase (for both qubits and qudits). We further explore these questions and the properties of the sharpening transition in a future work [57], where we give evidence that the N_0-sharpening transition corresponds to a percolation of exactly sharp regions that occurs within the true charge-sharp phase.

Using a scaling ansatz $N_0 = f[(p - p_\#)L^{1/\nu_\#}]$, we find the best collapse for $\nu = 1.3 \pm 0.15$, consistent with the entanglement data of the qubit. We also look at the evolution of N_0 with t/L in Fig. 8. We find that N_0 goes to 1 for all p at long times, but the rate of increase of N_0 decreases with L for $p < p_\#$ and increases with L for $p > p_\#$, while remaining constant for $p = p_\#$. We check that the exponent ν and the critical probability $p_\#$ do not vary much with the time chosen for calculating N_0 as long as it is not too large. The crossing value of N_0 tends to increase with increasing t/L: We focus here on the regime where the thermodynamic limit is taken first so t/L is "small" (in practice, $t/L = 2$ is small enough to obtain stable results). We thus conclude that the volume- to area-law transition of $[S_n]$ in the qubit sector can be interpreted as a charge-sharpening transition wherein starting from a mixed superposition of all charge sectors, the measurements collapse the wave function to one charge sector for $p > p_\# = 0.315 \pm 0.01$.

3. Local ancilla probe

As in Sec. III for the qubit-only ($d = 1$) model, we now present a scalable probe of the charge-sharpening transition

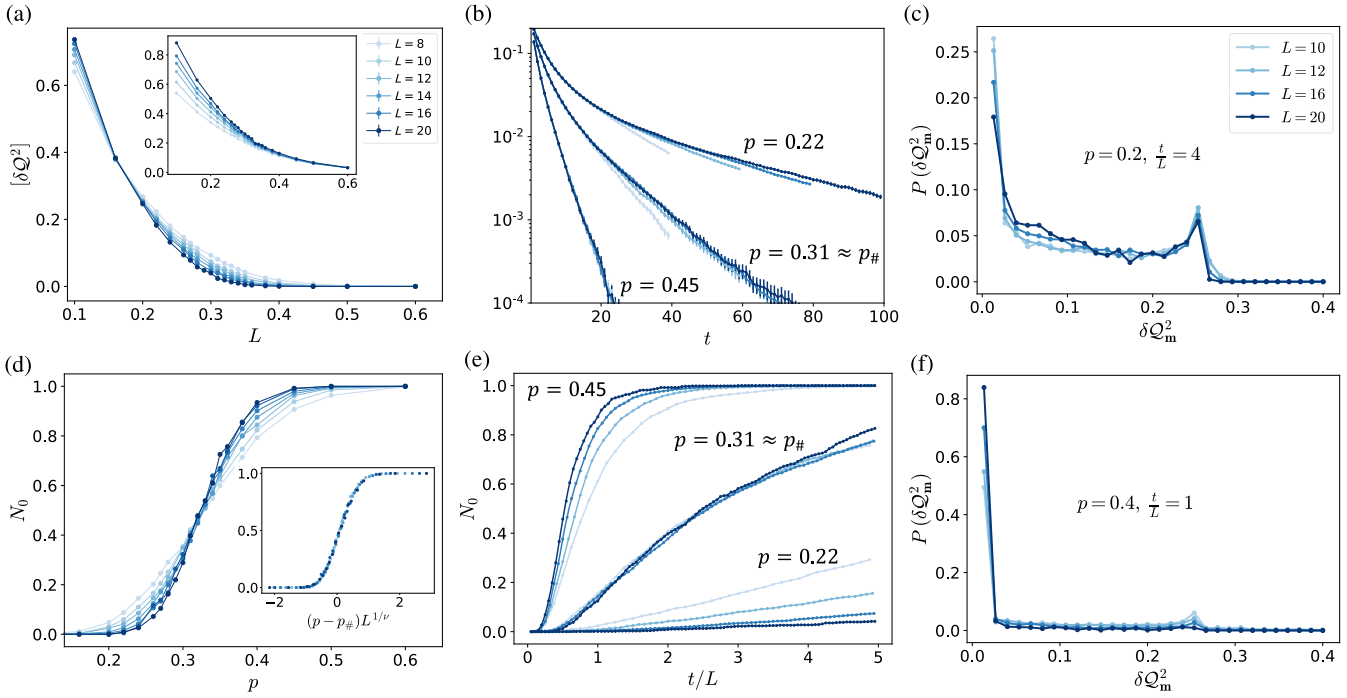

FIG. 8. Charge-sharpening transition in the statistical mechanics model. (a) Plot of $[\delta\mathcal{Q}^2]$ versus p plotted for $t/L = 2$. We find that with increasing L the value of $[\delta\mathcal{Q}^2]$ approaches zero for $p > p_\# \approx 0.3$. This is consistent with the entanglement transition in the qubit sector where we observed area-law scaling for $\langle S_n \rangle$ for $p > p_\#$. Inset: charge variance in half of the system. (b) Charge variance $[\delta\mathcal{Q}^2]/L$ versus time t. For $p \lesssim p_\#$, $[\delta\mathcal{Q}^2]/L$ decays exponentially with a decay rate decreasing with L. For $p > p_\#$, the decay rate is the same for all L suggesting that $\langle \sigma^2 \rangle / L$ goes to zero faster with increasing system size (faster in units of t/L). (c) Histogram of the charge variance in the charge-fuzzy phase. (d) Plot of N_0 versus p with finite size collapse in the inset. N_0 was calculated at $t/L = 2$. We find excellent collapse for $p_\# = 0.315$ and $\nu = 1.3$. (e) Time evolution of N_0. We clearly see a reversal in trend with system size L around $p_\# \approx 0.31$. At the transition $p = p_\#$ we find that $N_0 \sim h(t/L)$, with $h(x)$ some scaling function, consistent with a dynamical exponent $z = 1$. (f) Histogram of the charge variance in the charge-sharp phase. The peak at 0.25 is due to trajectories with superposition of two charge sectors $\mathcal{Q}$ and $\mathcal{Q} + 1$. The peak is stronger, and more stable, in the fuzzy phase than in the sharp phase. Error bars in (a) and (b) are obtained from the error of the mean using standard deviations.

by entangling a reference ancilla qubit to different charge sectors $|\Psi_0\rangle = |\psi_\mathcal{Q}\rangle|0\rangle + |\psi_{\mathcal{Q}-1}\rangle|1\rangle$. Our numerical protocol is identical to that of Sec. III (Fig. 9). Those results are obtained by taking the minimal cut to be always at the link connecting the ancilla to the system: this is correct in the thermodynamic limit below the percolation threshold $p < p_c = 1/2$, and removes spurious finite size effects due to percolation physics. Our results for this quantity are qualitatively different from the $d = 1$ model of Sec. III, which showed a possible crossing in that quantity, while we observe here a behavior consistent with that of an order parameter for the charge-sharpening transition. This difference might be due to different "magnetization" exponents β, with the $d = 1$ model being closer to percolation. Analogous to the N_0 quantity defined above, we introduce N_{pure} which is equal to the number of trajectories where the reference qubit is purified. We observe a crossing N_{pure} near $p_\# \approx 0.315$ and plot the finite size collapse in Fig. 9.

To conclude this section we compare our results for the charge-sharpening transition in the two limits of $d = 1$ and $d \to \infty$. In both cases we have found Lorentz invariant critical points with $z = 1$ to within numerical accuracy. In the limit of $d \to \infty$ we have a correlation length exponent $\nu_\# = 1.3 \pm 0.15$, which is consistent with the percolation universality class that is also found in the qudit sector at $p_c = 1/2$. Whereas in the limit of $d = 1$ we have $\nu_\# \approx 2$, which points to a unique universality class that is distinct from that in the limit of $d \to \infty$, and the entanglement transition at p_c.

B. Entanglement dynamics

Finally, we briefly turn to the dynamics of the Rényi entropies $S_n(t)$ using the statistical model. As before, S_n is the contribution of the U(1) qubits to the entanglement entropy: the total entropy S_n^T always grows linearly for $p < p_c = 1/2$ due to the qudit sector. The results below should be interpreted as subleading corrections to the growth of the total entanglement entropy arising due to the slow dynamics of the U(1) qubits.

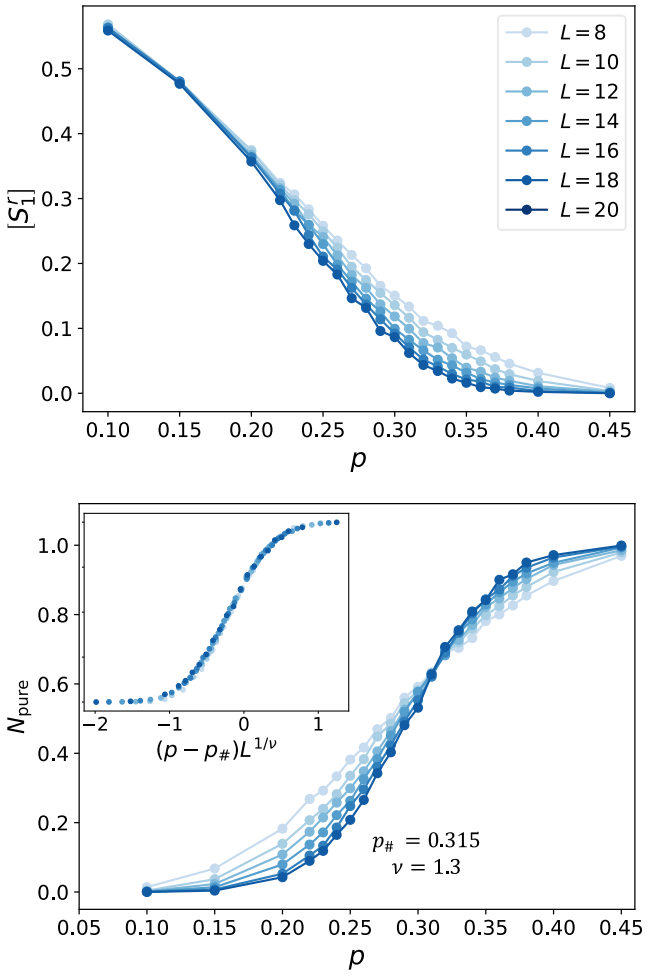

FIG. 9. Ancilla probe in the statistical mechanics model. Top: entanglement entropy of the ancilla qubit, which behaves as an order parameter for the charge-sharpening transition. Bottom: finite size scaling of the number of trajectories where the ancilla qubit is purified N_{pure}, probing the charge-sharpening transition.

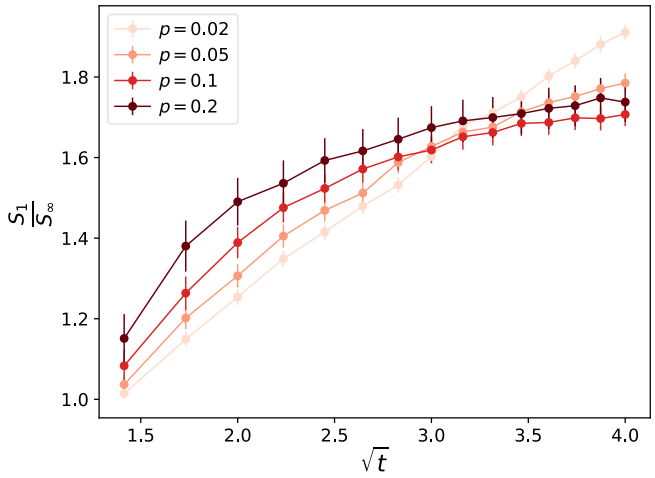

FIG. 10. Entanglement dynamics in the statistical mechanics model. Ratio $R_s = (S_1/S_\infty)$ versus $\sqrt{t}$ for $L = 12$. We find that R_s saturates implying that S_∞ and S_1 are growing at the same rate $\sim t$. As expected, the saturation time is longer at low p. Error bars are from error in mean using standard deviations and standard error propagation.

In the absence of measurements, the statistical mechanics model predicts that all Rényi entropies scale diffusively $S_{n>1} \sim \sqrt{t}$, whereas $S_{n=1} \sim t$, in agreement with earlier results [52,54,62] (see Appendix C 1). As argued in Sec. II, in the presence of measurements, the "dead regions" responsible for this unusual behavior survive only until a time $t \sim p^{-2/3}$ in typical trajectories. At long times, the overlap of the wave function with dead regions is zero, and we expect the trajectory-averaged Rényi entropies $[S_n]$ to grow linearly in time for all $p > 0$.

To confirm this, we plot the ratio $R_s = [S_1]/[S_\infty]$ in Fig. 10. The average von Neumann entropy $[S_1]$ is expected to grow linearly for all p. The quantity R_s is thus a measure of the growth of $[S_\infty]$: if $[S_\infty]$ were to increase as $\sqrt{t}$, then we would expect R_s to grow as $\sqrt{t}$, too. This is indeed what we observe at $p = 0$. At higher p we find that R_s saturates to a constant value implying that $[S_1] \sim [S_\infty] \sim t$, in agreement with our general argument. Other observables confirming this scaling are presented in Appendix C 1.

VI. DISCUSSION

In this work, we have studied measurement-induced phases and phase transitions in monitored quantum circuits with charge conservation. We argued that measurements can have a dramatic effect on entanglement growth. While all Rényi entropies with index $n > 1$ grow diffusively in the absence of measurements, for any $p > 0$, the effect of these rare regions are washed out by measurements leading to ballistic scaling $S_n \sim t$ at long times.

Whereas, in the absence of symmetry, there can only be two possible steady states, entangling or purifying, charge conservation enriches this dynamical phase diagram. We uncovered a new type of charge-sharpening transition that separates distinct entangling phases. Even as the dynamics remain scrambling and lead to a volume-law entangled state, the U(1) charge can either be fuzzy or sharp depending on the rate of measurements. This charge-sharpening transition occurs at a critical measurement rate $p_\#$ that is generically smaller than p_c, corresponding to the purification transition. This new transition is also fundamentally different from the purification entanglement transition, as for any $p > 0$, the charge will eventually become sharp with exponentially small corrections for $t \gg t_\# \sim L$ (up to logarithmic corrections) for a system of size L, whereas the purification time diverges exponentially in the system size in the entangling phases. The sharpening timescale for U(1) circuits is also parametrically much faster than that in $\mathbb{Z}_2$ symmetric circuits [47] (linear versus exponential), highlighting the fundamental difference between scrambling

of U(1) and $\mathbb{Z}_2$ symmetric modes. Thus the measurement-induced phases inside the volume law for U(1) systems are conceptually very different than those in $\mathbb{Z}_2$ symmetric systems [47]. The type of sharpening transitions studied here is unique to systems with diffusive modes.

We presented evidence for the existence of this transition using both exact numerical results in a symmetric qubit model ($d = 1$) and from the numerical analysis of an emergent statistical mechanics model describing the evolution of charged qubits coupled to large qudits ($d \to \infty$). For the model in the $d \to \infty$ limit, the correlation length exponent ν of the charge-sharpening transition is consistent with that of percolation. In contrast, in the qubit-only model we showed that the charge-sharpening correlation length exponent is distinct from that found for the entanglement transition with $\nu_{\#} \approx 2$. Understanding the critical properties of this transition represents a clear challenge for future works. A conceivable scenario could be that the charge-sharpening and entanglement transitions could merge into a single transition below a critical qudit dimension, $d < d_c$. Establishing on firmer grounds the existence of a distinct charge-sharpening transition would also be an important task for future works.

The statistical mechanics model is also an important step in the understanding of symmetric monitored circuits. We were able to take the replica limit analytically, which is a crucial step to uncover key properties of measurement-induced phase transitions and is often the most daunting challenge in the studies of monitored circuits [47]. We find that the contribution of the U(1) degrees of freedoms to the Renyi entropies is related to the entropy of local charge fluctuations along the minimal cut [Eq. (19)]. Though this mapping is restricted to the $d \to \infty$ limit, since the permutation degrees of freedom are gapped in the volume-law phase, we do not expect them to change the general structure of the phase diagram or the universality class of the sharpening transition for finite d. This is an important distinction with the $d \to \infty$ percolation limit of the entanglement transition [19,20], where $1/d$ corrections are relevant and completely modify the simple percolation picture.

The statistical mechanics approach can also be readily generalized to arbitrary Abelian symmetries (Appendix B), thus providing a controlled platform for future studies of symmetric circuits, for example, $\mathbb{Z}_n$ circuits. We emphasize that the change of perspective in treating the measurements as quenched disorder rather than annealed [19,20] is crucial in incorporating symmetric or constrained degrees of freedom in the statistical mechanics model. Recently, this change of perspective turned out to also be useful in other contexts, for example, in the study of negativity in non-symmetric circuits [74].

In the models we consider in this paper, the measurements kill both entanglement and charge fluctuations. This is especially natural for the qubit-only model which is perhaps physically more relevant. In principle, we can consider various modifications of this simple model. For example, in thecase of the qudits model, one could consider different rate or strength of measurements for the U(1) and neutral degrees of freedom, or measurement-only models where measurements compete against creating and destroying charge fluctuations. A detailed study of such models is left out for future work, although we do not expect any qualitative change to the physics of the charge-sharpening transition discussed in this paper.

We mostly focused on the global properties of charge dynamics, and defer local properties of the steady state to future work [57]. An effective field-theory description of the statistical mechanics model introduced above predicts that the local sharpening transition is in a Kosterlitz-Thouless (KT) universality class [57]. In this picture, the fuzzy phase corresponds to the quasi-long-range order and the charge-sharp phase is the symmetric phase [57]. A proper analysis of the replica limit is however crucial to uncover the peculiar nature of this transition, including the dynamical properties distinguishing the phases; see Ref. [57]. It would be interesting to look for signatures of such KT scaling in the qubit model ($d = 1$), even though KT criticality is notoriously hard to study in finite size numerics.

The conservation law has not affected the universality class of the entanglement transition in the limit of $d \to \infty$. Whereas, in the limit of $d = 1$ we have shown that the log scaling of the Renyi entropy at criticality $S_n \sim \alpha(n) \log L$ has an $\alpha(n)$ that is clearly distinct from the transition with Haar-random gates [28], which implies that the (boundary)universality class is distinct in the presence of a conservation law. Interestingly, we have found that $\nu \approx 1.3$, which is not sensitive enough to discern between percolation, stabilizer dynamics, and the Haar universality class. It will be interesting in future work to probe other critical exponents of the entanglement transition with a conservation law to discern other unique properties of this transition.

It would also be interesting to extend our results to other symmetry groups or kinetic constraints. Our results can be readily generalized to arbitrary Abelian groups (see Appendix B). As we discuss in Appendix B, if one assumes the existence of charge-sharp phases for other symmetry groups and spatial dimensionalities, standard duality relations [75] immediately imply the existence of monitored random circuit classes that exhibit volume-law-entangled phases with symmetry-breaking, symmetry-protected topological, and intrinsic topological orders in a typical trajectories. Such trajectory-ordered but volume-law-entangled phases are clearly forbidden in any equilibrium or closed-system dynamical setting, and are a new feature of nonunitary open-system dynamics.

Moreover, it is clear by now that new types of dynamical phases can be obtained in the steady state of monitored

quantum circuits, from the combination of different competing (noncommuting) measurements and unitary dynamics [29–32]. The full phase structure allowed by the microscopic symmetry group and the dynamical symmetries of such monitored quantum circuit appears to be particularly rich [47], and remains largely unexplored. We expect non-Abelian symmetries to be especially interesting, as they could lead to fundamental constraints on the entanglement structure of the steady state, as in the case of many-body localized systems [76].

ACKNOWLEDGMENTS

We thank Michael Gullans, David Huse, Chaoming Jian, Vedika Khemani, and Andreas Ludwig for useful discussions and collaborations on related projects. We acknowledge support from NSF DMR-1653271 (S. G.), NSF DMR-1653007 (A. C. P.), the U.S. Air Force Office of Scientific Research under Grant No. FA9550-21-1-0123 (R. V.), and the Alfred P. Sloan Foundation through Sloan Research Fellowships (A. C. P., J. H. P., and R. V.). A. Z. and J. H. P. are partially supported by Grant No. 2018058 from the United States–Israel Binational Science Foundation (BSF), Jerusalem, Israel. A. Z. is partially supported through a Fellowship from the Research Discovery Informatics Institute. The Flatiron Institute is a division of the Simons Foundation.

APPENDIX A: MAPPING TO THE STATISTICAL MODEL WITH U(1) QUBITS

In this appendix, we present a detailed discussion of the mapping to the statistical model, and derive Eq. (19) in the limit $d \to \infty$. To evaluate the quantities in Eq. (14), we need to calculate the average of $\mathcal{K} \equiv K_{\mathbf{m}}^{\otimes Q} \otimes K_{\mathbf{m}}^{\dagger \otimes Q}$, corresponding to Q copies of the random circuit. Each unitary gate in $\mathcal{K}$ is repeated Q times, and since they are drawn independently we can individually average them over the random unitary ensemble. Let us denote the tensor product of Q copies of a gate by $\mathcal{U} \equiv U^{\otimes Q} \otimes U^{\dagger \otimes Q}$. We view $\mathcal{U}$ as a superoperator which acts on two sites with each leg containing Q ket states and Q bra states; let $|g^i \alpha^i\rangle\langle g^{i*} \alpha^{i*}|$ be a basis where g^i is a basis of the qudit Hilbert space $\mathbb{C}^d$ and α^i is the computational basis for the qubit. The index i labels replicas, and runs from 1 to Q. Using standard Haar calculus and Weingarten formulas, we find that the action of $\bar{\mathcal{U}}$ on the above basis is nontrivial after averaging if and only if $g^{i*} = g^{\sigma(i)}$ and $\alpha^{i*} = \alpha^{\sigma(i)}$, where $\sigma \in \mathcal{S}_Q$ is a permutation. Therefore, we introduce a shorthand notation for writing the relevant members of the basis as

$$(g^i \alpha^i; \sigma) \equiv |g^i \alpha^i\rangle\langle g^{\sigma(i)} \alpha^{\sigma(i)}|. \tag{A1}$$

More precisely, each unitary gate in the circuit is replaced by a vertex associated with a pair (corresponding to ingoing and outgoing legs) of permutation "spins" $\sigma, \bar{\sigma}$, each belonging to the permutation group $\mathcal{S}_Q$. In the $d \to \infty$ limit, these spins become locked together in a single permutation degree of freedom σ_a that we associate with that vertex. Vertices from adjacent gates, i.e., those which share an input or output qubit and qudits, are connected by links in a way that will be explained below. In the large-d limit, the weight associated with a vertex in the partition function is given by $V_a = 1/D^Q$, where D is the size of the block of the relevant symmetry sector. We have $D = d^2$ if all incoming and outgoing charges are the same, and $D = 2d^2$ otherwise; see Eq. (3).

The results for $\bar{\mathcal{U}}$ to leading orders are summarized in Fig. 6; the subleading corrections are suppressed as $\mathcal{O}(1/d^2)$, which we ignore in rest of the paper. The factor of $\delta_{\alpha_1^i \beta_1^i} \delta_{\alpha_2^i \beta_2^i} + \delta_{\alpha_1^i \beta_2^i} \delta_{\alpha_2^i \beta_1^i}/2$ in Fig. 6 enforces U(1) charge conservation, and follows from the size of the different blocks in Eq. (3). In fact, if we view charge 0 as vacuum and charge 1 as a particle, then the dynamics of the U(1) degree of freedoms can be understood as hard-core random walks of these particles, known as the symmetric exclusion process. Alternatively, it can be seen as a special case of the 6-vertex model [see Fig. 6(b)]. Though we have focused mainly on the case of U(1) symmetry groups, our approach readily extends to other Abelian groups. In Appendix B we provide a general derivation for arbitrary Abelian symmetry groups.

1. Link weights

Combining Fig. 6 with the brick wall geometry of the circuit leads to a model described on a square lattice as shown in Fig. 11. Each vertex has an element from the permutation group $\mathcal{S}_Q$ and each link has Q copies of the elements of the basis of the local Hilbert space. The vertex weights V_a are given by the rule described in Fig. 6(b). The link weight W_{ab} has two kinds of contributions: (1) due to the presence of domain wall in the permutation group elements $\sigma_{a,b}$ (DW constraint) and (2) the state at the link $\langle ab \rangle$ is being measured (measurement constraint). We describe these constraints in detail in the following.

(1) *DW constraint.*—We first consider a link joining two vertices that we label "1" and "2." If we integrate out the qudit degrees of freedom, we find the following weight for the links:

$$\begin{aligned} W_{12}(\sigma_2^{-1}\sigma_1) &= \sum_{g_1^i, g_2^i} \mathrm{Tr}[(g_1^i \alpha_1^i; \sigma_1)(g_2^i \alpha_2^i; \sigma_2)^\dagger] \\ &= d^p \delta_{C_1} \ldots \delta_{C_p}, \end{aligned} \tag{A2}$$

where $C_1 \ldots C_p$ is the cycle structure of the permutation element $\sigma_2^{-1}\sigma_1$, p is the number of cycles in that permutation, and δ_{C_i} is equal to 1 if all charge states of the replicas within cycle C_i are the same, and otherwise equal to 0. Note that we cannot sum

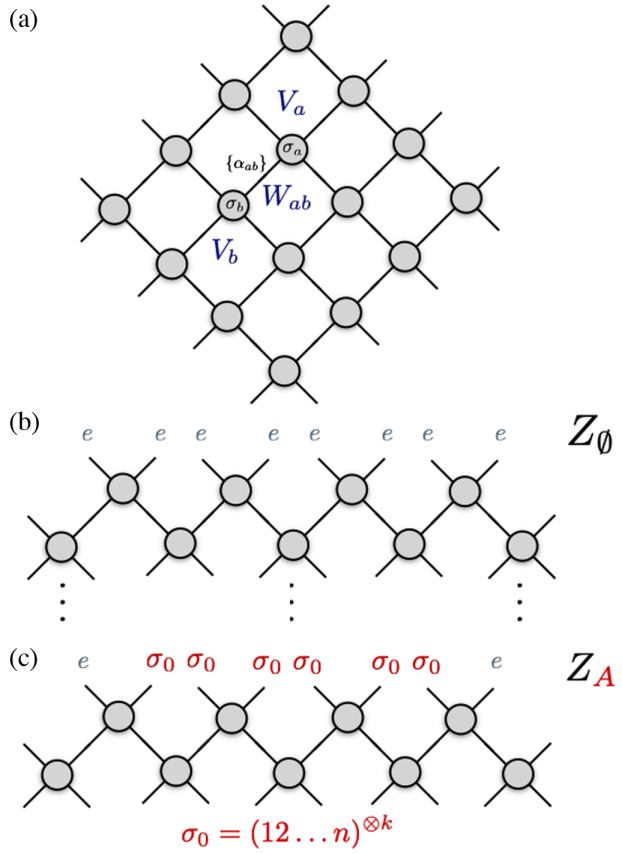

FIG. 11. Replicated statistical mechanics model. (a) The replicated statistical model is defined on a tilted square lattice, with permutation degrees of freedom $\sigma_a \in \mathcal{S}_Q$ living on vertices, and charge degrees of freedom $\{\alpha^i\}_{i=1,\ldots,Q}$. The Boltzmann weights have contributions from both vertices V_a, see Eq. (A10), and links W_{ab}, Eq. (A9). (b) Fixed boundary conditions in $Z_\emptyset$ at the top layer (ending the circuit at a given time t), with all permutations fixed to e. (c) The partition function Z_A differs from $Z_\emptyset$ by the boundary condition fixed to σ_0 in the entanglement interval A. This creates a domain wall that follows a minimal cut in the limit $d \to \infty$.

over the charges α^i as these depends on the states at neighboring links (see Fig. 6).

Intuitively we can interpret the above result as follows. Since the link is shared between vertices with different permutations σ_1 and σ_2, then we must have the following constraint,

$$(g^i\alpha^i;\sigma_1) = (g^i\alpha^i;\sigma_2), \tag{A3}$$

which is true if and only if $\sigma_2^{-1}\sigma_1(\{\alpha_i\}) = \{\alpha_i\}$, and $\sigma_2^{-1}\sigma_1(\{g_i\}) = \{g_i\}$. Let us take the simple case where $\sigma_2^{-1}\sigma_1$ is equal to a transposition, say, (12). We can interpret the above equation as saying that $g_1 = g_2$ and $\alpha_1 = \alpha_2$. The $g_1 = g_2$ condition will reduce the number of allowed basis qudit states from d^Q to d^{Q-1}, and since all qudit contributes equally, the weight of the link in this case will be reduced by a factor $1/d$ due to the reduced configurational entropy in the qudit sector. For the qubit degrees of freedom, we cannot sum over all spins due to the nonlocal charge conservation constraint. The more general case of $\sigma_2^{-1}\sigma_1 \in \mathcal{S}_Q$ follows similarly, giving Eq. (A2). An important thing to note is that each transposition in $\sigma_2^{-1}\sigma_1$ reduces the weight by $1/d$ and the weight is strongest when $\sigma_2 = \sigma_1$, that is when there is no DW—corresponding to a ferromagnetic interaction. Thus at large-d limit, it is expensive to have a DW and the system will remain in an ordered phase unless DW are forced, for example, at the entanglement cut (see Fig. 11). This will play an important role in the subsequent discussion.

(2) *Measurement constraint.*—If the link $\langle 12\rangle$ happens to be measured, then the measurement outcomes are the same in all replicas; that is, all copies are acted on with the same projection operator. If the projection operator is denoted as $P = P^q \otimes P^d$, then we have the weight

$$W_{12}(\sigma_2^{-1}\sigma_1;P) = \mathrm{Tr}[(g_2^i\alpha_2^i;\sigma_2)^\dagger P^{\otimes Q}(g_1^i\alpha_1^i;\sigma_1)P^{\otimes Q}]. \tag{A4}$$

Averaging over all measurement outcomes results in

$$\begin{aligned} W_{12} &= \sum_{s=0,1}\sum_{x=1,\ldots,d} W_{12}(\sigma_2^{-1}\sigma_1;P_s^q \otimes P_x^d) \\ &= d\sum_{s=0,1}\prod_i \delta_{\alpha^i,s}, \end{aligned} \tag{A5}$$

where $\delta_{\alpha^i,s}$ ensures that the charge state of the ith replica is compatible with the measurement outcome $s = 0,\ 1$ of the qubit. Whenever a measurement occurs, all Q charges on the corresponding link are constrained to be same. This gives the δ factor in Eq. (A5). For the qudit sector, this leads to a decrease in configurational entropy from d^Q to d. An important observation is that the link weights W_{ab} do not depend on the permutation $\sigma_b^{-1}\sigma_a$, a result of crucial importance for the discussion below.

2. Replicated model

Combining all these results we can write a statistical model with the partition function given by

$$Z = \sum_{\mathbf{m}} Z[\mathbf{m}], \tag{A6}$$

$$Z[\mathbf{m}] = \sum_{\text{configurations}} \left(\prod_{(ab)\in\text{links}} \prod_{v\in\text{vertices}} W_{ab}(\sigma_b^{-1}\sigma_a)V_v \right), \tag{A7}$$

where $\sum_{\mathbf{m}} \equiv \sum_{\{\mathbf{X}\}} p^{N_\mathbf{X}}(1-p)^{LT-N_\mathbf{X}} \sum_{\{\mathcal{M}(\mathbf{X})\}}$, where $\mathbf{X}$ denotes a configuration of measurement locations, $N_\mathbf{X}$ is the number of links being measured (number of bonds in the percolation configuration $\mathbf{X}$), L is the spatial length of the system, T is the number of time steps, and $\mathcal{M}(\mathbf{X})$ is the set of qubit measurement outcomes at measurement locations $\mathbf{X}$. The sum over configurations is given by

$$\sum_{\text{configurations}} \equiv \sum_{\{\sigma_v\}\in\mathcal{S}_Q} \sum_{\{\alpha^1\}=0,1} \cdots \sum_{\{\alpha^Q\}=0,1} \equiv \sum_{\{\sigma_v\}\in\mathcal{S}_Q} \sum_{\{\alpha\}}, \tag{A8}$$

corresponding to permutation and charge degrees of freedom in each replica. The link weights W_{ab} are given by

$$W_{ab}(\sigma_b^{-1}\sigma_a) = \begin{cases} d^{|\sigma_b^{-1}\sigma_a|-Q}\delta_{C_1}\ldots\delta_{C_{|\sigma_b^{-1}\sigma_a|}} & \text{if } (ab) \text{ not in } \mathbf{X} \\ d^{1-Q}\delta_{\alpha^i,s_{ab}} & \text{if } (ab) \text{ in } \mathbf{X}, \end{cases} \tag{A9}$$

with $s_{(ab)} \in \mathcal{M}(\mathbf{X})$ the measurement outcome of the qubit on link (ab). Finally, the vertex weight V_v is given by

$$V_v = \prod_{i=1}^{Q} \frac{\delta_{\alpha_1^i\beta_1^i}\delta_{\alpha_2^i\beta_2^i} + \delta_{\alpha_1^i\beta_2^i}\delta_{\alpha_2^i\beta_1^i}}{2} = \prod_{i=1}^{Q} V_v^i, \tag{A10}$$

where $\alpha_{1,2}$ and $\beta_{1,2}$ are incoming and outgoing charges (see Fig. 6). We note that V_v factorizes over the replicas, that is, $V_v = \prod_{i=1}^{Q} V_v^i$; this will play an important role in factorizing $Z[\mathbf{m}]$ in the discussion below.

Note that we have integrated out the qudit sector from the model. This was possible due to each qudit on a given link being independent of the values at other links. However, this is not possible for the U(1) sector on account of nonlocal constraints due to the charge conservation. Importantly, the statistical model $Z(\mathbf{m})$ should be thought of as a quenched disordered model where the measurement locations and outcomes (for the qubit) are quenched "impurities"; averaged quantities in the original problem have become quenched average in the statistical model. From now on, $\mathbf{m} = \{\mathbf{X}, \mathcal{M}(\mathbf{X})\}$ will denote the system's quantum trajectory with measurement locations and U(1) measurement outcomes fixed, corresponding to a fixed "disorder" realization of the statistical model. This is unlike the previous works on the nonsymmetric problem where the randomness in the measurement locations was absorbed in the statistical model in an annealed way.

3. Replica limit

We now proceed to take the replica limit, and will use various notations summarized in Table I.

TABLE I. Summary of the meaning of various notations used in this appendix.

α_l^i	Charge at link l and copy i
$\{\alpha^i\}$	Set of charges on all links for copy i
$\{\alpha_l\}$	Set of charges on link l for all copies
$\{\alpha\}$	Set of charges on all links and copies
$\delta_{\{\alpha\}}^{\{l\}}$	All copies of α on set of links $\{l\}$ are equal
$\delta_{\{\alpha\},\{\mathcal{M}\}}^{\{l\}}$	All copies of $\{\alpha\}$ on links $\{l\}$ are equal to $\{\mathcal{M}\}$

We first focus on the partition function $Z_\varnothing(\mathbf{m})$, where the links at the top boundary are restricted to be of the form $(g^i\alpha^i; e)$. The permutation identity element e represents the fact that we are tracing over all the system and is equal to the Born probability of observing the particular trajectory $\mathbf{m}$. As mentioned above, a DW in the statistical model is suppressed by $1/d^{Q-p}$, where p is the number of cycles in the DW. Thus, the leading order contribution to $Z_\varnothing$ comes when all vertex elements are equal to e. This simplifies $Z_\varnothing(\mathbf{m})$ dramatically, as we do not need to sum over the permutation elements. We have

$$Z_\varnothing(\mathbf{m}) = d^{(1-Q)N_m}\left(\sum_{\{\alpha\}=0,1} \delta_{\{\alpha\},\mathcal{M}(\mathbf{m})}^{\mathbf{m}} \prod_v V_v\right),$$

where N_m is the number of measured links, $\delta_{\{\alpha\},\mathcal{M}(\mathbf{m})}^{\mathbf{m}}$ is nonzero and equal to 1 if and only if the charges $\{\alpha\}$ on the measured sites are equal to the measurement outcomes $\mathcal{M}(\mathbf{m})$ of the qubit, and V_v is given in Eq. (A10). Intuitively, we should only sum over charge configurations compatible with the measurement outcomes. The partition function can be factorized over replicas to give

$$Z_\varnothing(\mathbf{m}) = d^{(1-Q)N_m}(Z_\varnothing^{(1)}(\mathbf{m}))^Q, \tag{A11}$$

where $Z_\varnothing^{(1)}(\mathbf{m})$ is given by

$$Z_\varnothing^{(1)}(\mathbf{m}) = \sum_{\{\alpha\}} \delta_{\{\alpha\},\mathcal{M}(\mathbf{m})}^{\mathbf{m}} \prod_v V_v^{(1)}. \tag{A12}$$

The superscript (1) denotes the fact that the quantity is for a single replica.

We can similarly factorize $Z_A(\mathbf{m})$ with the caveat that we now have a minimal cut for the permutation degrees of freedom running through the system (see discussion in Sec. IV A). A DW between e and $(1\ldots n)^{\otimes k}$ reduces the link weight by $d^{k+1-Q} = d^{-(n-1)k}$ [Eq. (A9)], and the contribution of the cut to the partition function is thus given by $d^{-(n-1)k\ell_{\mathrm{DW}}}$, where ℓ_{DW} is the length of the minimal cut. There are $k+1$ cycles in the DW: k cycles of the type

$(1\ldots n)$ and the last one being an identity on a single copy. Thus, we can factorize $Z_A(\mathbf{m})$ as

$$Z_A(\mathbf{m}) = d^{(1-Q)N_m-(n-1)k\ell_{\mathrm{DW}}} \times \sum_{\{\alpha^i\}=0,1} \delta^{\mathbf{m}}_{\{\alpha\},\mathcal{M}(\mathbf{m})} \prod_{C_a} \delta^{\mathrm{DW}}_{\{\alpha^{C_a}\}} \prod_v V_v, \tag{A13}$$

where $\delta^{\mathrm{DW}}_{\{\alpha^{C_a}\}}$ is nonzero (and equal to 1) if and only if the charges within the cycle C_a are the same on (unmeasured) links on the minimal cut. We can further factorize the above equation to get

$$Z_A(\mathbf{m}) = d^{(1-Q)N_m-(n-1)k\ell_{\mathrm{DW}}} (Z_A^{(n)}(\mathbf{m}))^k Z_\varnothing^{(1)}(\mathbf{m}), \tag{A14}$$

where

$$\begin{aligned} Z_A^{(n)}(\mathbf{m}) &= \sum_{\{\alpha\}} \delta^{\mathrm{DW}}_{\{\alpha\}} \prod_{i=1}^{n} \left(\delta^{\mathbf{m}}_{\{\alpha^i\},\mathcal{M}(\mathbf{m})} \prod_v V_v^i \right) \\ &= \sum_{\beta_1\ldots\beta_{\ell_{\mathrm{DW}}}} \prod_{i=1}^{n} \left(\sum_{\{\alpha^i\}} \delta^{\mathrm{DW}}_{\{\alpha^i\},\{\beta\}} \delta^{\mathbf{m}}_{\{\alpha^i\},\mathcal{M}(\mathbf{m})} \prod_v V_v^i \right) \\ &\equiv \sum_{\{\beta\}} Z_A[\mathbf{m};\{\beta\}]^n, \end{aligned} \tag{A15}$$

with $\delta^{\mathrm{DW}}_{\{\alpha\},\{\beta\}}$ nonzero (and equal to 1) if and only if all copies of charges on the unbroken (not measured) links along the minimal cut are equal to $\{\beta\}$. The superscript (n) denotes the fact that we have n charge copies. Using the above results and Eq. (13), we find

$$S_n(\mathbf{m}) = \frac{-1}{n-1} \lim_{k\to 0} d^{(1-Q)N_m} Z_\varnothing^{(1)}(\mathbf{m}) \times \frac{d^{-(n-1)k\ell_{\mathrm{DW}}} (Z_A^{(n)})^k - (Z_\varnothing^{(1)})^{nk}}{k}. \tag{A16}$$

Remarkably, this factorized form allows us to take the replica limit *exactly*:

$$\begin{aligned} S_n(\mathbf{m}) &= \frac{-1}{n-1} Z_\varnothing^{(1)}(\mathbf{m}) \ln \frac{Z_A^{(n)}}{(Z_\varnothing^{(1)})^n} + \ell_{\mathrm{DW}} \ln d \\ &= \frac{-1}{n-1} Z_\varnothing^{(1)}(\mathbf{m}) \ln \left(\sum_{\{\beta\}} \frac{Z_A[\mathbf{m};\{\beta\}]^n}{(Z_\varnothing^{(1)})^n} \right) + \ell_{\mathrm{DW}} \ln d, \end{aligned} \tag{A17}$$

where $\{\beta\}$ represents all possible configuration of the charge on the unmeasured links along the minimal cut. We can further think of $Z_A[\mathbf{m};\{\beta\}]/(Z_\varnothing^{(1)})$ as the probability for the charges along the unbroken links of the minimal cut to be equal to $\{\beta\}$ in the statistical model described by the partition function $Z_\varnothing^{(1)}$. Denoting this probability by $p_{\{\beta\}}$, we have our final result:

$$S_n(\mathbf{m}) = \frac{-1}{n-1} Z_\varnothing^{(1)}(\mathbf{m}) \ln \left(\sum_{\{\beta\}} p_{\{\beta\}}^n \right) + \ell_{\mathrm{DW}} \ln d. \tag{A18}$$

4. $p = 0$ limit

To illustrate the meaning of the statistical model (A18), we compute S_n for $p = 0$. Let us start from the following product state:

$$|\psi_0\rangle = (a_0|0\rangle + a_1|1\rangle)^{\otimes L}. \tag{A19}$$

In terms of the statistical model, this corresponds to the bottom links being in charge states 1 or 0 with probability a_1^2 and a_0^2, respectively. The minimal cut will be spatial in nature as we are considering late times and $\ell_{\mathrm{DW}} = L_A$ since the permutations are fully ordered. Since the vertex weights (A10) are SU(2) symmetric, the link charge states are invariant under time evolution. This immediately gives $p_{\{\beta\}} = a_0^{2N_0} a_1^{2N_1}$, where $N_{0,1}$ are the number of links with charge 0,1 in $\{\beta\}$. Using Eq. (A18), we find the following expression for the Rényi entropies at late times:

$$S_n = \frac{-1}{n-1} \ln(|a_0|^{2n} + |a_1|^{2n})^{L_A} + L_A \ln d. \tag{A20}$$

This result is consistent with thermalization to a density matrix $\rho_A = e^{-\mu\mathcal{Q}}/\mathrm{Tr}e^{-\mu\mathcal{Q}}$, where the chemical potential μ is set by charge conservation:

$$\langle \mathfrak{q} \rangle = a_1^2 = \mathrm{Tr}[\mathfrak{q}\rho_A] = \frac{e^{-\mu}}{1+e^{-\mu}}. \tag{A21}$$

We check that the Rényi entropies are indeed given by $S_n = -1/(n-1) \ln \mathrm{Tr}\rho_A^n$, since

$$S_n = L_A \left(\ln d + \frac{1}{n-1} \ln[\langle \mathfrak{q} \rangle^n + (1 - \langle \mathfrak{q} \rangle))^n] \right), \tag{A22}$$

which coincides with Eq. (A20).

5. Charge variance

In this section, we briefly discuss evaluating the charge variance $[\delta\mathcal{Q}^2]$ in the language of the statistical model discussed above. The charge variance for fixed measurement locations and outcomes is given by $\delta\mathcal{Q}^2_{\mathbf{m}} = \langle \mathcal{Q}^2 \rangle_{\mathbf{m}} - \langle \mathcal{Q} \rangle^2_{\mathbf{m}}$. As the first term is linear in $\rho_{\mathbf{m}}$, the average over measurement outcomes will give a trivial answer at infinite temperature (see point 3 in Sec. II B). We have

$$[\langle \mathcal{Q}^2 \rangle] = \mathrm{Tr}\mathcal{Q}^2/\mathrm{Tr}\mathbb{I} = L(L+1)/4,$$

where charges take value 0 and 1. Any nontrivial physics is hidden in the second term. Nevertheless, the distribution of the variance over various trajectories is an interesting

quantity, and it will be useful to evaluate this quantity using the replica trick.

We first consider the second term, which is given by

$$[\langle\mathcal{Q}\rangle^2] = \sum_{\mathbf{m}} \mathbb{E}_U \left[p_{\mathbf{m}} \left(\frac{\mathrm{Tr}(\mathcal{Q}\rho_{\mathbf{m}})}{\mathrm{Tr}\rho_{\mathbf{m}}} \right)^2 \right].$$

We can use the replica trick to rewrite the above expression as

$$\begin{aligned}[\langle\mathcal{Q}\rangle^2] &= \lim_{k\to 0} \sum_{\mathbf{m}} \mathbb{E}_U \{ [\mathrm{Tr}(\mathcal{Q}\rho_{\mathbf{m}})]^2 (\mathrm{Tr}\rho_{\mathbf{m}})^{2k-1} \} \\ &= \lim_{k\to 0} \sum_{\mathbf{m}} \mathbb{E}_U [\mathrm{Tr}\rho_{\mathbf{m}}^{\otimes(2k+1)} T], \end{aligned} \tag{A23}$$

where T is an operator acting on the $2k+1$ copies at the top boundary and is given by $T = \mathcal{Q}\otimes\mathcal{Q}\otimes\mathbb{I}\ldots\otimes\mathbb{I}$. As discussed above, the above quantity maps to a classical statistical model on averaging over random unitary gates U. Since the action of T does not mix different copies, we can factorize the contribution of different copies as in Sec. A 3. The resulting expression, after taking the replica limit, is given by

$$[\langle\mathcal{Q}\rangle^2] = \sum_{\mathbf{m}} Z_{\varnothing}^{(1)}(\mathbf{m}) \langle\mathcal{Q}_T\rangle_{\mathbf{m},\mathrm{stat}}^2, \tag{A24}$$

where $\langle\cdot\rangle_{\mathrm{stat}}$ is the average in the statistical model described by the partition function $Z_{\varnothing}^{(1)}(\mathbf{m})$ [see Eq. (A12)], and the subscript T in $\mathcal{Q}$ is to denote the fact that it is a quantity defined on the top boundary. As mentioned before, there is no simple expression for $[\langle\mathcal{Q}\rangle^2]$, but we can use the statistical mechanics model to evaluate it numerically. Similarly, for $\langle\mathcal{Q}^2\rangle_{\mathbf{m}}$ the top operator T is given by $T = \mathcal{Q}^2\otimes\mathbb{I}\ldots\otimes\mathbb{I}$, and we have

$$[\langle\mathcal{Q}^2\rangle] = \sum_{\mathbf{m}} Z_{\varnothing}^{(1)}(\mathbf{m}) \langle\mathcal{Q}_{\mathrm{T}}^2\rangle_{\mathbf{m},\mathrm{stat}}. \tag{A25}$$

APPENDIX B: STATISTICAL MECHANICS MODEL FOR GENERAL ABELIAN SYMMETRIES

In this appendix, we generalize the statistical mechanics models to general Abelian groups and discuss consequences of charge-sharp phases under duality transformations. Notably, our results suggest the existence of volume-law-entangled phases with symmetry-protected and intrinsic topological order.

1. Haar average

Consider a general Abelian group G, with $\alpha \in \{1\ldots|R|\}$ labeling the different combinations of total charge for pairs of sites [e.g., for the U(1) model $\alpha \in \{-1,0,+1\}$, for $\mathbb{Z}_N$ $\alpha \in \{0\ldots N-1\}$, etc.]. We can decompose a symmetric two-site unitary into a direct sum of reps: $U = \sum_\alpha U_\alpha P_\alpha$, where P_α is a projector onto the αth charge-sector subspace. The main object in the statistical mechanics model is the unitary average of $\mathbb{E}_U[U^Q \otimes U^{*Q}]$, where Q is the number of replicas, which decomposes into a direct sum of all R^{2Q} charge-sector combinations. Since Haar averaging requires that each U_α is "paired" with a complex-conjugated partner U_α^* of the same total charge, only terms in which the U^{*Q} charge sectors form a permutation of the U^Q charge sectors contribute. For each of these surviving combinations of charge sectors, denote by n_α the number of times that charge sector α appears in U^Q, and choose permutation elements $\sigma,\tau \in S_Q$ that sort the Q replicas into groups of the same charge.

Then we can write

$$\begin{aligned}\mathbb{E}_U[U^Q\otimes U^{*Q}] = \sum_{n_{1\ldots R}:\sum_\alpha n_\alpha = Q} \sum_{\sigma,\tau\in \frac{S_Q}{S_{n_1}\times\ldots\times S_{n_R}}} W_{\sigma,\tau} \bigotimes_\alpha \mathbb{E}_U (U_\alpha^{n_\alpha} P_\alpha^{n_\alpha} \\ \otimes U_\alpha^{*n_\alpha} P_\alpha^{*n_\alpha}) W_{\sigma,\tau}^\dagger, \end{aligned} \tag{B1}$$

where $W_{\sigma,\tau}$ is the unitary acting on $\mathcal{H}^q\otimes\mathcal{H}^{*q}$ that permutes the Q copies of U by σ and the Q copies of U^* by τ, and the permutation elements σ, τ range over the quotient group $S_Q/S_{n_1}\times\cdots S_{n_R}$ to avoid overcounting equivalent permutations that cycle identical replicas with the same charge sector. Here we have labeled projectors acting on $\mathcal{H}^*$ with an asterisk simply for readability, and this mark carries no mathematical content.

The Haar average of each charge-sector-group is $\mathbb{E}_U(U_\alpha^{n_\alpha}\otimes U_\alpha^{*n_\alpha}) = \sum_{\sigma_\alpha,\tau_\alpha\in S_{n_\alpha}} \mathrm{Wg}_{Dd^2}(\sigma_\alpha^{-1}\tau_\alpha; n_\alpha) |\sigma_\alpha\rangle\!\rangle\langle\!\langle\tau_\alpha|$, where Wg is the Weingarten function, D_α is the number of states in the charge sector α, and $|\sigma\rangle\!\rangle$ denotes the operator which permutes the input legs of U by σ, and contracts them with the corresponding legs of U^* (and similarly for $\langle\!\langle\sigma|$ acting on the output legs). For our purposes, we will only need the large-d limit:

$$\lim_{d\to\infty} \mathrm{Wg}_d(\sigma^{-1}\tau; Q) \sim \frac{1}{d^Q}\delta_{\sigma,\tau}. \tag{B2}$$

The sum over the total charge-sector permutations σ_α can now be combined with the quotient-group permutations σ, τ to yield a simpler sum over S_Q permutations:

$$\begin{aligned}\mathbb{E}_U[U^Q\otimes U^{*Q}] = \frac{1}{d^{2Q}} \sum_{\alpha_1\ldots\alpha_Q} \prod_i D_{\alpha_i}^{-1} \sum_{\sigma\in S_Q} P_{\alpha_1}\otimes\cdots\otimes P_{\alpha_Q} \\ \otimes P^*_{\alpha_{\sigma(1)}}\otimes\cdots\otimes P^*_{\alpha_{\sigma(Q)}} |\sigma\rangle\!\rangle \\ \times \langle\!\langle\sigma| P_{\alpha_1}\otimes\cdots\otimes P_{\alpha_Q}\otimes P^*_{\alpha_{\sigma(1)}}\otimes\cdots\otimes P^*_{\alpha_{\sigma(Q)}}. \end{aligned} \tag{B3}$$

Note that the two sets of projectors are partly redundant since $P_\alpha^2 = P_\alpha$, and since $P_\alpha\otimes\mathbb{1}|\sigma\rangle\!\rangle = \mathbb{1}\otimes P_{\alpha_{\sigma(i)}}|\sigma\rangle\!\rangle$, but

are written in this way to emphasize that charge is separately conserved in each replica, and also that the charge-sector labels on the $\mathcal{H}^*$ spaces are related to those in the $\mathcal{H}$ spaces by the permutation element σ.

Though complicated in appearance, Eq. (B3) has a simple interpretation: each gate becomes a vertex in the statistical mechanics model labeled by (i) a permutation element $\sigma \in S_Q$ and (ii) Q-different total charge-sector labels (those of the conjugate copies are related by permutation), which can be conveniently associated with the Q-different individual link charges. After averaging, the indices of the gate input and output are unrelated, except by total charge conservation in each replica. Hence any input charge configuration can be transferred with equal weight $\sim 1/D_\alpha$ to any outgoing charge configuration with the same total charge α. The remaining rules for domain wall and measurement constraints closely parallel those of the U(1) model described above.

a. Example: $\mathbb{Z}_2$ symmetric monitored circuits

As an example, consider a random monitored circuit ensemble with symmetry group $G = \mathbb{Z}_2$, consisting of qubits with $\mathbb{Z}_2$ symmetry charge $\mathfrak{q}_i = (1+\sigma_i^x)/2 \in \{0,1\}$, and charge addition rule $\mathcal{Q} = \sum_i \mathfrak{q}_i$ mod 2 (each accompanied by large dimension qudits that transform trivially under the symmetry). The effective statistical mechanics model in the $d \to \infty$ limit is an "8-vertex" model, which has an additional two vertices compared to the U(1)/6-vertex case that respectively correspond to pair creation and annihilation of charges, and differs also in that all eight vertices come with weight $v = 1/2$.

b. Example: $\mathbb{Z}_N$ symmetric monitored circuits

As a second example, we can consider models with symmetry group $G = \mathbb{Z}_N$ for general N consisting of "qunits" with charge basis states $\{|0\rangle, \ldots, |N-1\rangle\}$ having symmetry charge $\mathfrak{q} = 0 \ldots N-1$ (again, each accompanied by large-d qudits). The resulting statistical mechanics model would be an N^3-vertex model, with N different groups of vertices corresponding to the N different total charges, and each group has N different ways to apportion the incoming charge between the two input legs, and N different ways to apportion it between the output legs, each weighted by a factor of $v = 1/N$.

From these examples, one can readily generalize to arbitrary finite Abelian groups for which G can be written as a product of different $\mathbb{Z}_N$ factors.

2. Dual entangling phases classical and quantum orders

In principle, the statistical mechanics models sketched above can be simulated by sign-problem-free Monte Carlo simulations for arbitrary Abelian symmetry groups and dimensions. Though we have only performed systematic numerics on the U(1) symmetric models in one dimension, we hypothesize that the resulting physics and phase diagram is similar for other Abelian symmetry groups and higher dimensions. Assuming this hypothesis holds, then standard duality transformations would relate these simple symmetric monitored random circuit models to those with more complex types of phases including symmetry-protected topological (SPT) phases and discrete gauge theories.

In the following, we denote a system with n spatial dimensions and one time dimension as $(n+1)d$, where d should not be confused with the dimension of the qudits. In all the examples we discuss here, there will only be a single type of measurement. Generalizing the statistical mechanics framework to multiple types of incompatible measurements remains an open challenge for future work, and to date has only been done for Clifford circuit models [29–32]. The $1+1d$ examples with $\mathbb{Z}_2$ symmetries were extensively explored in Ref. [47] from a related but different perspective, and many aspects of the physics we discuss below echo that work (though we do not consider possible phases arising from additional replica permutation symmetries as it is not clear whether these can be realized in the physical replica limit).

a. $1+1d$: Symmetry protected topology

In $1+1d$, discrete symmetry groups of the form $\mathbb{Z}_m \times \mathbb{Z}_n$ have nontrivial projective representations and can protect topological phases [77,78] when m and n have a nontrivial greatest common divisor. These SPT phases can be mapped (at the level of local operators) onto trivial paramagnets by a "decorated domain wall" mapping [79], which attaches conjugate operators that add (remove) a $\mathbb{Z}_n$ charge to the left (right) of the $\mathbb{Z}_m$ symmetry generator. For example, with $G = \mathbb{Z}_2^A \times \mathbb{Z}_2^B$ represented on a dimerized chain of spin $1/2$'s with the two $\mathbb{Z}_2$ factors acting on the A and B sublattices, respectively, the duality mapping is generated by unitary transformation $U_{\text{dual}} = e^{-i\pi/4 \sum_i \sigma_i^z (\sigma_{i-1}^z + \sigma_{i+1}^z)}$ (which commutes with the symmetry, but is not generated by a symmetric Hamiltonian). U_{dual} interchanges the stabilizers of a trivial paramagnet with those of the cluster state SPT: $\sigma_i^x \to \sigma_{i-1}^z \sigma_i^x \sigma_{i+1}^z$.

How would the charge-sharp and charge-fuzzy phases of the $\mathbb{Z}_2$ symmetry circuit model transform under this duality? To answer this question, note that the total charge in a region of length ℓ maps onto the string-order parameter of length ℓ for the SPT phase. For example, in the $G = \mathbb{Z}_2^A \times \mathbb{Z}_2^B$ example, the $\mathbb{Z}_2^A$ interval charge maps onto $\sigma_{2i-1}^z (\prod_{i=1}^{\ell} \sigma_{2i}^x) \sigma_{2(i+\ell)+1}^z$. In the charge-sharp phase, the interval charge at fixed time in a single trajectory has nonzero expectation value that is asymptotically independent of ℓ (i.e., charge fluctuations satisfy an area law). Correspondingly, in the dual model, there is a long-range string-order parameter in each trajectory. We note that, while the string order has a nonvanishing expectation value at any fixed time slice in the dual-charge-sharp phase, this

expectation value will vary from time slice to time slice due to intermediate evolution causing short-range charge fluctuations across the end of the string.

While it is perhaps not surprising that in the area-law phase with SPT order can be stabilized at large measurement rates (in this dual mapping the original charge measurements become projections onto the stabilizers of the SPT phase), the possibility of a volume-law-entangled phase with SPT order in a fixed trajectory does not have any precedent in equilibrium, and represents a fundamentally new type of phenomenon that relies essentially on both nonequilibrium and nonunitary evolution.

b. $1+1d$: Spontaneous symmetry breaking

By a closely related reasoning to the section above, applying standard Kramers-Wannier (KW) duality (which exchanges the paramagnetic and spontaneous symmetry broken phases) to a $1+1d$ $\mathbb{Z}_N$ symmetric random circuit model relates a charge-sharp phase to a dual phase with long-range symmetry breaking order in a given trajectory; i.e., the KW duality exchanges sharp and fuzzy phases. For example, for a $\mathbb{Z}_2$ symmetric circuit duality (KW) mapping exchanges $\sigma_i^x \leftrightarrow \sigma_i^z\sigma_{i+1}^z$.

c. $2+1d$: Discrete gauge theories

As a final application, we consider KW dualities in $2+1d$ systems, which map models with global symmetries onto dual "pure" gauge theories that have gauge magnetic-flux degrees of freedom but lack dynamical electrical charge. In this mapping, the original site degrees of freedom, which live on vertices of a square lattice and transform under a $\mathbb{Z}_N$ symmetry, map to dual link variables residing on a dual lattice whose sites are centered on plaquettes of the original lattice. Symmetry domain wall operators map onto $\mathbb{Z}_N$ electric field operators living on links, and local symmetry generators map onto the $\mathbb{Z}_N$ flux through the dual plaquette. We define the duality mapping to act trivially on the large-d qudits, which in the dual lattice now reside at the center of plaquettes.

This duality mapping interchanges symmetry charge in the original variables with gauge magnetic flux in the dual variables. Hence, the charge-sharp and charge-fuzzy phases respectively map onto confined and deconfined phases of the gauge theory. Namely, in the charge-sharp phase, the total charge in a region Σ, $\mathcal{Q}_\Sigma$, has fluctuations only from local quantum fluctuations near the boundary $\partial\Sigma$. In the dual mapping, $\mathcal{Q}_\Sigma$ transforms into a Wilson loop around the boundary, which we write schematically as $W_\Sigma = e^{i\oint_{\partial\Sigma}\mathbf{A}\cdot d\boldsymbol{\ell}}$ (where e^{iA} is the conjugate variable to the $\mathbb{Z}_N$ electric field, and all continuum notations should be appropriately interpreted as lattice sums). Thus, in a given trajectory at late times, the dual of the charge-sharp and fuzzy phases is characterized by area- or volume-law scaling of Wilson loops, respectively,

$$\lim_{t\to\infty}[|\langle\psi_{\mathbf{m}}(t)|W_\Sigma|\psi_{\mathbf{m}}(t)\rangle|] \sim \begin{cases} e^{-|\partial\Sigma|} & \text{dual charge sharp} \\ e^{-|\Sigma|} & \text{dual charge fuzzy,} \end{cases} \tag{B4}$$

i.e., correspond to confined and deconfined phases, respectively. Note here, as for spin-glass-like order parameters, it is important to take absolute values before averaging to obtain the area-law scaling.

Again, the prospect of a volume-law-entangled, but trajectory-deconfined gauge theory represents a new possibility not present in equilibrium settings or closed-system dynamics. We leave establishing the (non)existence of this phase and the study of potential critical properties of putative unconventional volume-law entangled confinement transitions as a loose end for future study. Other potentially interesting generalizations include both gauge theories with electrically charged matter, which are not dual to systems with global symmetries, and continuous U(1) gauge invariant random circuit dynamics, for which the duality omits monopole instantons that are known to confine equilibrium gauge theories in $2+1d$, but perhaps have a different fate in monitored random circuit dynamics.

APPENDIX C: ADDITIONAL NUMERICAL RESULTS

1. Entanglement dynamics in the statistical mechanics model

In this appendix, we present additional results on the entanglement dynamics obtained from the statistical mechanics model.

We start with the $p=0$ case, and analyze how the argument for $\sqrt{t}$ growth translates to the statistical model language. We are working in the regime where $L \gg t$, so the minimal cut runs along the time direction. For simplicity of the argument, we assume that the cut does not fluctuate and is exactly vertical; that is, the cut passes through the same link at all times (we checked that our results are independent from averaging over fluctuations of the minimal cut). Using Eq. (19), the Rényi entanglement entropies are related to the classical Rényi entropies for charge configurations along the minimal cut. Let us denote this distribution by P_{DW}, with $S_\infty = \ln p_{\max}$, where $p_{\max}$ is the maximum of P_{DW}. We find that $p_{\max}$ is given by $P_{\mathrm{DW}}(0\ldots0) \equiv P_0$. P_0 is the probability for all charges on the vertical cut to be equal to 0 [equivalently, we could have also considered $P_{\mathrm{DW}}(1\ldots1) \equiv P_1$]. P_0 describes the part of the dynamics where there is no exchange of charge across the cut and is therefore dominated by dead regions in the initial state, which we know to be the source of the dominant contribution in the Schmidt values. As we discussed in Sec. II, if the initial state has a dead region of size $\sqrt{t}$ centered at the entanglement cut, charges cannot diffuse to the cut until times of order t, so the

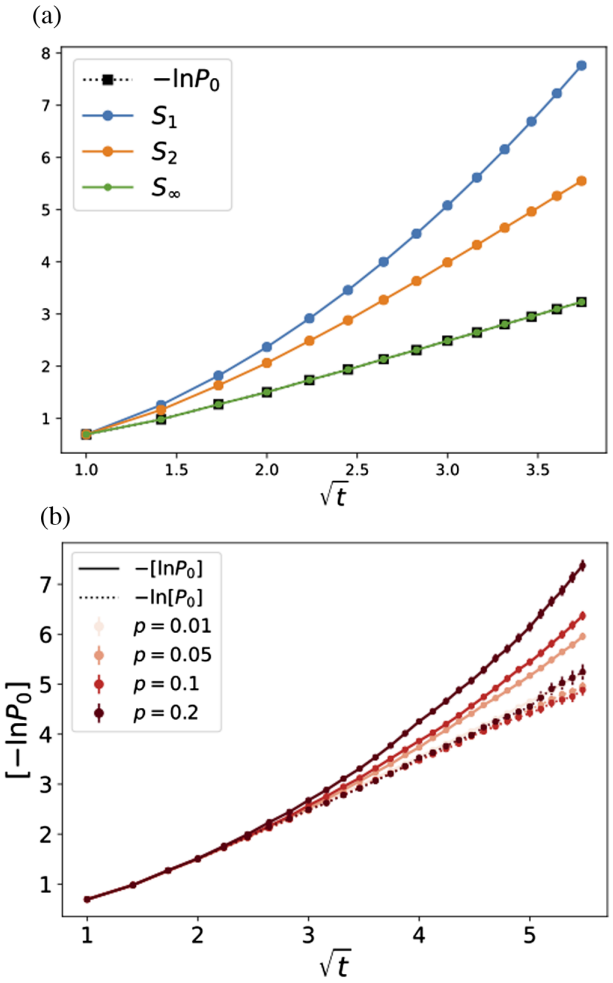

FIG. 12. Entanglement dynamics in the statistical mechanics model. (a) Plot of S_1, S_2, S_∞, and $-\ln P_0$ versus $\sqrt{t}$ for $p = 0$ obtained using the statistical model with a fixed vertical minimal cut. We clearly see different growth of S_1 and S_∞, S_2. The curve of $-\ln P_0$ exactly overlaps the S_∞ curve as argued in the main text. (b) Plot showing $[-\ln P_0]$ versus $\sqrt{t}$ for various p, and $L = 12$. We find that this quantity grows linearly with time for any nonzero p. We also plot the average $-\ln[P_0]$ for various p (dashed curves), which grows as $\sqrt{t}$ independently of p. Error bars are obtained using standard deviations.

configurational entropy of charge along the vertical minimal cut will remain zero. It follows that $P_0 \geq \exp(-\sqrt{Dt})$ and therefore that $S_n \leq \sqrt{Dt}$ for $n > 1$. Meanwhile, typical components of the initial wave function give rise to essentially random charge configurations on the minimal cut. Owing to the greater multiplicity of typical configurations they dominate S_1, which grows linearly in t. These expectations are borne out in Fig. 12(a).

We now turn to $p > 0$. For $p > 0$, the charge on measured sites in a given trajectory is constrained to match the measurement outcome. As we noted in Sec. II, this suffices to eliminate dead regions in typical trajectories. To capture the effect of dead regions on the growth of S_∞ for $p > 0$, we calculate $-\ln P_0$ as a proxy for entanglement entropies. For numerical convenience, we make two simplifying assumptions: (1) we ignore fluctuations of the minimal cut and (2) we do not perform measurements on links adjacent to the cut (this avoids numerically expensive postselection procedures as the trajectories with nonzero P_0 quickly become rare as we increase p).

We plot $[-\ln P_0]$ and $-\ln[P_0]$ versus $\sqrt{t}$ in Fig. 12(b). We find that the quantity $-\ln[P_0]$ grows as $\sqrt{t}$ for all p. This is expected because we are averaging over the trajectories before calculating the (pseudo)entropy; this is the same as in the $p = 0$ case where the unitary evolution can be seen as equivalent to doing the sum over all trajectories. We find that at low p, $[-\ln P_0]$ stays closer to the $\sqrt{t}$ growth for longer times. At higher p it diverges significantly and crosses over to linear growth. Though $[-\ln P_0]$ is not exactly equal to the Rényi entropy, this transition from $\sqrt{t}$ to linear growth $\sim t$ is a generic phenomenon for all quantities where the survival of dead regions becomes a rare occurrence due to measurements, consistent with the general argument in Sec. II and the results of Sec. V.

2. Charge-sharpening dynamics in the fuzzy phase and near the charge-sharpening transition

In this appendix, we present numerical evidence that the charge sharpens on a timescale $t_\# \sim L$, in agreement with the general argument of Sec. II. We plot the fraction N_0 of trajectories with $\delta\mathcal{Q}^2 < \epsilon$ versus $t \sim L$, both in the qubit chain numerics (Fig. 13) and in the statistical mechanics model (Fig. 14). We observe a clear crossover when N_0 lifts off from zero on a timescale scaling linearly with L, as expected. Note that this sharpening timescale $t_\# \sim L/p$ is much smaller than the purification timescale $t_\pi \sim e^L$ [16].

We now turn to the critical dynamics near the charge-sharpening phase transition in qubit chains. Before

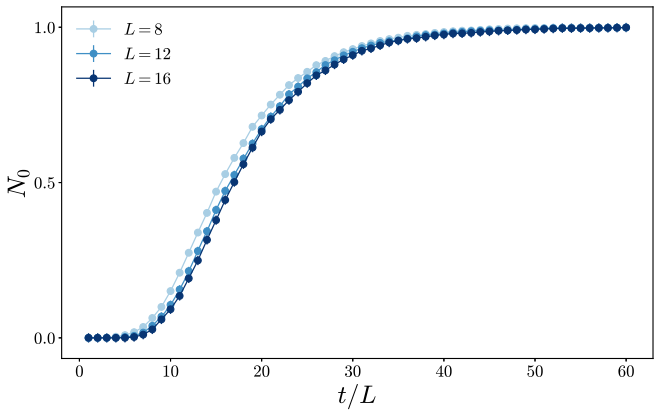

FIG. 13. Dynamics of charge sharpening in qubit chains. Fraction of trajectories with $\delta\mathcal{Q}^2 < \epsilon$ with $\epsilon = 10^{-3}$ at $p = 0.085$, inside the fuzzy phase.

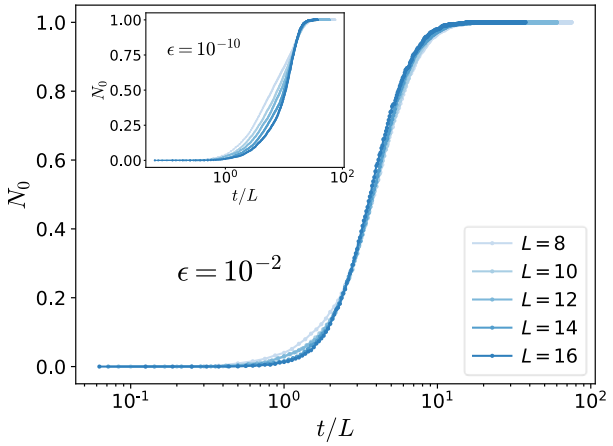

FIG. 14. Dynamics of charge sharpening in the statistical model. Fraction of trajectories with $\delta\mathcal{Q}^2 < \epsilon$ with $\epsilon = 10^{-2}$ at $p = 0.24$, inside the fuzzy phase. Inset: different threshold $\epsilon = 10^{-10}$, showing a similar scaling of the charge sharpening over a timescale $t \sim L$.

embarking into numerical details, we summarize the physics of the critical dynamics obtained from the simulations.

For generic initial states that mix multiple charge sectors, the charge sharpening happens in two stages. The measurement first sharpens the charge from multiple sectors to two consecutive sectors $(N, N+1)$. The measurement then further collapses the superposition of the two sectors $(N, N+1)$ to a unique charge (either N or $N+1$). The two stages are separated by the crossover time $t_\# \sim L/p$. At much later times $t \gg t_\#$ we find $N_0 \to 1$ in a critical manner that we now turn to.

The numerical simulations of qubit chains suggest that the second stage is governed by charge-sharpening criticality. In the longtime limit, $t \gg t_\#$, we find that the universal scaling law for the critical dynamics is an exponential function,

$$O(t,p) \sim A_O(x) e^{-t/\xi_t(x)}, \quad \text{where } x \equiv (p - p_\#) L^{1/\nu_\#}. \tag{C1}$$

L is the system size and O is an observable sensitive to the criticality (e.g., N_0 and $S_{1,\mathcal{Q}}$). The universal decay rate ξ_t is a timescale that is different from the crossover time $t_\#$. Because of the spacetime symmetry, the timescale ξ_t follows a scaling law:

$$\xi_t(x)/L = B(x). \tag{C2}$$

Both universal scaling functions $A_O(x)$ and $B(x)$ are smooth in the critical regime. Right at the transition point, we obtain $\xi_t \approx 0.5 L/p_\#$.

We now show our numerical evidence to support the above physical picture. We present the charge variance distribution $\delta\mathcal{Q}^2$ in each phase and the vicinity of the charge-sharpening critical point in Fig. 15 to provide additional clarity on the nature of the charge-sharpening dynamics. More specifically, Fig. 15(a) is deep in the charge-fuzzy phase characteristic of the first stage of dynamics $t \ll t_\#$. It reveals a wide charge distribution, indicating that the quantum state at this stage is charge fuzzy and spreads across multiple sectors. The middle panel depicts the second stage $t > t_\#$ with $p \approx p_\#$. The charge variance at this stage is peaked at zero and 0.25, indicating the quantum state is either projected to a unique state or a superposition of two consecutive charge sectors $(N, N+1)$, respectively. The third panel is for latetime dynamics $t \gg t_\#$ deep in the charge-sharp phase. In this regime, only the peak near zero remains, indicating the longtime evolved quantum state has a unique sharp charge as expected.

We now focus on the critical dynamics of the charge-sharpening phase transition. We first present a strong evidence to show that the critical dynamics is only about two consecutive sectors $(N, N+1)$. In Fig. 16, we compare the dynamics of $1 - N_0$ to that of the ancilla-system entanglement entropy $S_{1,\mathcal{Q}}$ (see Sec. III B for the definition) in the vicinity of the transition point. The former involves multiple charge sectors, while the latter only involves two consecutive sectors $(N, N+1)$ (with $N = L/2$). After rescaling the overall amplitude, the longtime dynamics of $S_{1,\mathcal{Q}}$ almost perfectly matches with the second stage dynamics of $1 - N_0$, both going like $\sim e^{-t/\xi_t}$. Furthermore, due to the absence of other sectors, the ancilla probe saturates to the critical behavior much earlier than $1 - N_0$.

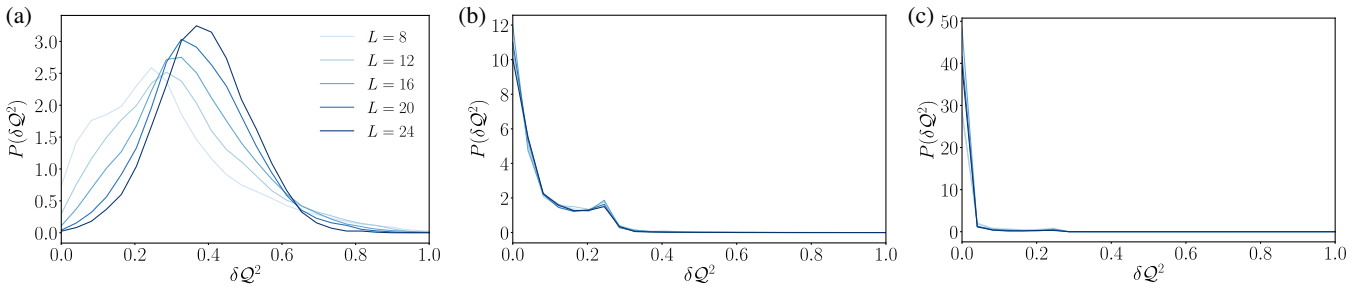

FIG. 15. Charge variance distribution in the qubit model. Distribution of the charge variance at $t/L = 4$ (a) in the charge-fuzzy phase $p = 0.05$, (b) near the critical point $p = 0.10$, and (c) in the charge-sharp phase $p = 0.14$.

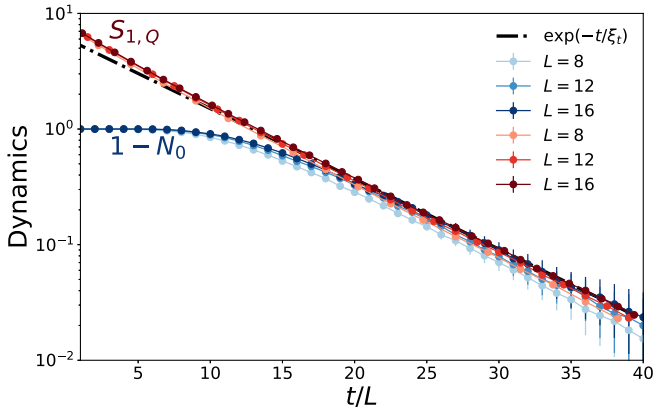

FIG. 16. Critical dynamics of charge-sharpening transition in qubit chains. Comparison of the dynamics of the ancilla entanglement entropy $S_{1,Q}$ and the quantity $1-N_0$, where N_0 is the fraction of trajectories with $\delta\mathcal{Q}^2 < 0.01$ and the ancilla entanglement entropy $S_{1,Q}$. After rescaling the overall amplitude, both observables collapse to the same exponential function in the longtime limit.

We thus conclude that the longtime critical dynamics only involves two consecutive sectors. In the longtime limit $t > t_{\#}$, both observables decay with the same exponential function, suggesting that the critical dynamics is exponential as in Eqs. (C1) and (C2).

We use the ancilla dynamics to establish the universal scaling functions $A_O(x)$ and $B(x)$ in Eqs. (C1) and (C2). The scaling function for the amplitude $A_O(x)$ depends on the choice of observable. It has been extracted for N_0 in Fig. 3(a) and for the ancilla probe $E_{1,Q}$ in Fig. 3(b). In this section, we extract the scaling of $B(x)$ for the universal decay rate. In Fig. 17, we calculate the longtime dynamics

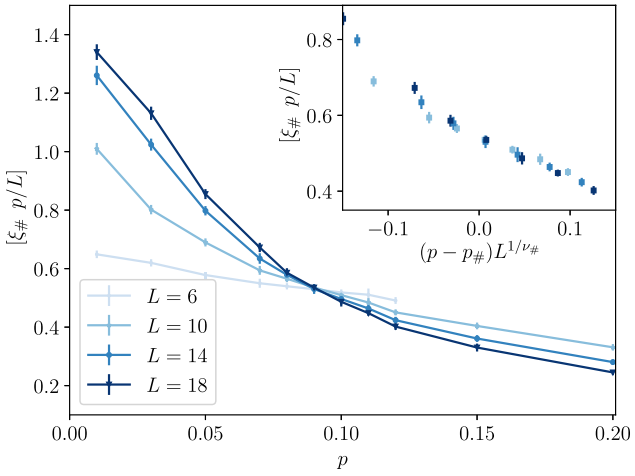

FIG. 17. Universal decay rate of charge-sharpening transition in qubit chains. Data and collapse of the decay rate in the vicinity of the charge-sharpening phase transition. The transition point $p = 0.088$ and the critical exponent $\nu = 2.15$ established in the main text are used to collapse the curves.

of $S_{1,Q}$ for various p and system sizes L, then fit the tail to extract the decay rate ξ_t. We find $\xi_t(p, L)$ cross at the transition point $p = p_{\#}$, indicating the existence of a scaling function $\xi_t(x)/L = B(x)$. To extract this function, we collapse the curves for different L using the transition point $p_{\#} = 0.088$ and the critical exponent $\nu_{\#} = 2.15$ established in Fig. 3(b).

APPENDIX D: FINITE SIZE SCALING

In the case of qubit chains ($d = 1$), the numerical simulations are performed for system sizes $L \leq 24$. We rely on finite size scaling protocols to extract the critical properties in the thermodynamic limit. We briefly explain the protocols in this appendix.

The quantities we studied in the main text, including the tripartite mutual information, the probability of a trajectory with certain charge variance, and the ancilla probes shown in Figs. 2 and 3, all have zero scaling dimension. In the vicinity of the transition point, they share the same finite size scaling ansatz:

$$R(p, L) = f\big((p - p_0)L^{1/\nu}, vL^{-\omega}\big) + \cdots, \tag{D1}$$

where L is the system size, and the measurement probability p is the relevant scaling field with a critical exponent $\nu > 0$. The transition point p_0 is either the entanglement phase transition p_c or the charge-sharpening phase transition $p_{\#}$.

To make the analysis systematic, we keep the leading irrelevant scaling variable v in the above scaling ansatz. In thermodynamic limit $L \to \infty$, it is suppressed by a nonnegative exponent ω. In finite size scaling, however, this field may play an important role. Numerically, we find that the variable v is significant for the ancilla probes while negligible for other quantities. We therefore have to use a more involved finite size scaling protocol as explained below to analyze the ancilla probes [80].

Since our numerics indicates that the scaling function $f(x, y)$ in Eq. (D1) is analytic for both $x = (p - p_0)L^{1/\nu}$ and $y = vL^{-\omega}$, one can approximate f with its Taylor expansion near the critical point,

$$R(p, L) = a_R + b_R(p - p_0)L^{1/\nu} + c_R(p - p_0)^2L^{2/\nu} + d_R/L^{\omega} + \cdots, \tag{D2}$$

where we assume p is close to the critical point p_0 and the system size is sufficiently large so that both $x = (p - p_0)L^{1/\nu}$ and $y = vL^{-\omega}$ are small. We also redefine the Taylor coefficient d_R to absorb the unknown amplitude v of the irrelevant variable. In the ideal case $d_R = 0$, $R(p_0, L)$ collapses to the universal constant a_R at the critical point. It indicates that the curves $R(p, L)$ for different system sizes perfectly cross at $p = p_0$. However, in realistic models, d_R is nonzero. The irrelevant

field then shifts the crossing points as the system size increases.

The ansatz Eq. (D2) allows us to extract the phase transition point p_0 and the critical exponent ν with the presence of a non-negligible irrelevant scaling variable. In practice, we collect dozens of data points for different p and system size L in the vicinity of the critical points. We then perform a nonlinear fitting with the ansatz Eq. (D2) by taking the coefficients a, b, c, d and critical properties p_0 and ν as the fitting parameters. Their error bars are defined as the standard error of the mean, which is approximately equal to a confidence interval of 67%. We then try to drop some of the parameters to make sure the fitting is robust and the error bars are reliable.

[1] Luigi Amico, Rosario Fazio, Andreas Osterloh, and Vlatko Vedral, *Entanglement in Many-Body Systems*, Rev. Mod. Phys. **80**, 517 (2008).

[2] Ryszard Horodecki, Paweł Horodecki, Michał Horodecki, and Karol Horodecki, *Quantum Entanglement*, Rev. Mod. Phys. **81**, 865 (2009).

[3] J. Eisert, M. Cramer, and M. B. Plenio, *Colloquium: Area Laws for the Entanglement Entropy*, Rev. Mod. Phys. **82**, 277 (2010).

[4] Pasquale Calabrese and John Cardy, *Entanglement Entropy and Conformal Field Theory*, J. Phys. A **42**, 504005 (2009).

[5] Nicolas Laflorencie, *Quantum Entanglement in Condensed Matter Systems*, Phys. Rep. **646**, 1 (2016).

[6] John Preskill, *Quantum Cmputing in the NISQ Era and Beyond*, Quantum **2**, 79 (2018).

[7] Adam Nahum, Jonathan Ruhman, Sagar Vijay, and Jeongwan Haah, *Quantum Entanglement Growth under Random Unitary Dynamics*, Phys. Rev. X **7**, 031016 (2017).

[8] Adam Nahum, Sagar Vijay, and Jeongwan Haah, *Operator Spreading in Random Unitary Circuits*, Phys. Rev. X **8**, 021014 (2018).

[9] C. W. von Keyserlingk, Tibor Rakovszky, Frank Pollmann, and S. L. Sondhi, *Operator Hydrodynamics, OTOCs, and Entanglement Growth in Systems without Conservation Laws*, Phys. Rev. X **8**, 021013 (2018).

[10] Tianci Zhou and Adam Nahum, *Emergent Statistical Mechanics of Entanglement in Random Unitary Circuits*, Phys. Rev. B **99**, 174205 (2019).

[11] Tibor Rakovszky, Frank Pollmann, and C. W. von Keyserlingk, *Diffusive Hydrodynamics of Out-of-Time-Ordered Correlators with Charge Conservation*, Phys. Rev. X **8**, 031058 (2018).

[12] Vedika Khemani, Ashvin Vishwanath, and David A. Huse, *Operator Spreading and the Emergence of Dissipative Hydrodynamics under Unitary Evolution with Conservation Laws*, Phys. Rev. X **8**, 031057 (2018).

[13] Yaodong Li, Xiao Chen, and Matthew P. A. Fisher, *Quantum Zeno Effect and the Many-Body Entanglement Transition*, Phys. Rev. B **98**, 205136 (2018).

[14] Brian Skinner, Jonathan Ruhman, and Adam Nahum, *Measurement-Induced Phase Transitions in the Dynamics of Entanglement*, Phys. Rev. X **9**, 031009 (2019).

[15] Soonwon Choi, Yimu Bao, Xiao Liang Qi, and Ehud Altman, *Quantum Error Correction in Scrambling Dynamics and Measurement-Induced Phase Transition*, Phys. Rev. Lett. **125**, 030505 (2020).

[16] Michael J. Gullans and David A. Huse, *Dynamical Purification Phase Transition Induced by Quantum Measurements*, Phys. Rev. X **10**, 041020 (2020).

[17] Yaodong Li and Matthew P. A. Fisher, *Statistical Mechanics of Quantum Error Correcting Codes*, Phys. Rev. B **103**, 104306 (2021).

[18] Ruihua Fan, Sagar Vijay, Ashvin Vishwanath, and Yi Zhuang You, *Self-Organized Error Correction in Random Unitary Circuits with Measurement*, Phys. Rev. B **103**, 174309 (2021).

[19] Yimu Bao, Soonwon Choi, and Ehud Altman, *Theory of the Phase Transition in Random Unitary Circuits with Measurements*, Phys. Rev. B **101**, 104301 (2020).

[20] Chao Ming Jian, Yi Zhuang You, Romain Vasseur, and Andreas W. W. Ludwig, *Measurement-Induced Criticality in Random Quantum Circuits*, Phys. Rev. B **101**, 104302 (2020).

[21] Yaodong Li, Xiao Chen, Andreas W. W. Ludwig, and Matthew P. A. Fisher, *Conformal Iinvariance and Quantum Nonlocality in Critical Hybrid Circuits*, Phys. Rev. B **104**, 104305 (2021).

[22] A. Zabalo, M. J. Gullans, J. H. Wilson, R. Vasseur, A. W. W. Ludwig, S. Gopalakrishnan, David A. Huse, and J. H. Pixley, *Operator Scaling Dimensions and Multifractality at Measurement-Induced Transitions*, Phys. Rev. Lett. **128**, 050602 (2022).

[23] Yaodong Li, Xiao Chen, and Matthew P. A. Fisher, *Measurement-Driven Entanglement Transition in Hybrid Quantum Circuits*, Phys. Rev. B **100**, 134306 (2019).

[24] Amos Chan, Rahul M. Nandkishore, Michael Pretko, and Graeme Smith, *Unitary-Projective Entanglement Dynamics*, Phys. Rev. B **99**, 224307 (2019).

[25] Xiangyu Cao, Antoine Tilloy, and Andrea de Luca, *Entanglement in a Free Fermion Chain under Continuous Monitoring*, SciPost Phys. **7**, 24 (2019).

[26] M. Szyniszewski, A. Romito, and H. Schomerus, *Entanglement Transition from Variable-Strength Weak Measurements*, Phys. Rev. B **100**, 064204 (2019).

[27] Michael J. Gullans and David A. Huse, *Scalable Probes of Measurement-Induced Criticality*, Phys. Rev. Lett. **125**, 070606 (2020).

[28] Aidan Zabalo, Michael J. Gullans, Justin H. Wilson, Sarang Gopalakrishnan, David A. Huse, and J. H. Pixley, *Critical Properties of the Measurement-Induced Transition in Random Quantum Circuits*, Phys. Rev. B **101**, 060301(R) (2020).

[29] Adam Nahum and Brian Skinner, *Entanglement and Dynamics of Diffusion-Annihilation Processes with Majorana Defects*, Phys. Rev. Research **2**, 023288 (2020).

[30] Matteo Ippoliti, Michael J. Gullans, Sarang Gopalakrishnan, David A. Huse, and Vedika Khemani, *Entanglement Phase Transitions in Measurement-Only Dynamics*, Phys. Rev. X **11**, 011030 (2021).

[31] Ali Lavasani, Yahya Alavirad, and Maissam Barkeshli, *Measurement-Induced Topological Entanglement Transitions in Symmetric Random Quantum Circuits*, Nat. Phys. **17**, 342 (2021).

[32] Shengqi Sang and Timothy H. Hsieh, *Measurement-Protected Quantum Phases*, Phys. Rev. Research **3**, 023200 (2021).

[33] Qicheng Tang and W. Zhu, *Measurement-Induced Phase Transition: A Case Study in the Nonintegrable Model by Density-Matrix Renormalization Group Calculations*, Phys. Rev. Research **2**, 013022 (2020).

[34] Javier Lopez-Piqueres, Brayden Ware, and Romain Vasseur, *Mean-Field Entanglement Transitions in Random Tree Tensor Networks*, Phys. Rev. B **102**, 064202 (2020).

[35] Adam Nahum, Sthitadhi Roy, Brian Skinner, and Jonathan Ruhman, *Measurement and Entanglement Phase Transitions in All-to-All Quantum Circuits, on Quantum Trees, and in Landau-Ginsburg Theory*, PRX Quantum **2**, 010352 (2021).

[36] Xhek Turkeshi, Rosario Fazio, and Marcello Dalmonte, *Measurement-Induced Criticality in $(2+1)$-Dimensional Hybrid Quantum Circuits*, Phys. Rev. B **102**, 014315 (2020).

[37] Yohei Fuji and Yuto Ashida, *Measurement-Induced Quantum Criticality under Continuous Monitoring*, Phys. Rev. B **102**, 054302 (2020).

[38] Oliver Lunt, Marcin Szyniszewski, and Arijeet Pal, *Measurement-Induced Criticality and Entanglement Clusters: A Study of One-Dimensional and Two-Dimensional Clifford Circuits*, Phys. Rev. B **104**, 155111 (2021).

[39] Oliver Lunt and Arijeet Pal, *Measurement-Induced Entanglement Transitions in Many-Body Localized Systems*, Phys. Rev. Research **2**, 043072 (2020).

[40] Sagar Vijay, *Measurement-Driven Phase Transition within a Volume-Law Entangled Phase*, arXiv:2005.03052.

[41] Xhek Turkeshi, Alberto Biella, Rosario Fazio, Marcello Dalmonte, and Marco Schiró, *Measurement-Induced Entanglement Transitions in the Quantum Ising Chain: From Infinite to Zero Clicks*, Phys. Rev. B **103**, 224210 (2021).

[42] Matteo Ippoliti and Vedika Khemani, *Postselection-Free Entanglement Dynamics via Spacetime Duality*, Phys. Rev. Lett. **126**, 060501 (2021).

[43] Tsung-Cheng Lu and Tarun Grover, *Spacetime Duality between Localization Transitions and Measurement-Induced Transitions*, PRX Quantum **2**, 040319 (2021).

[44] Chao-Ming Jian, Bela Bauer, Anna Keselman, and Andreas W. W. Ludwig, *Criticality and Entanglement in Non-Unitary Quantum Circuits and Tensor Networks of Non-Interacting Fermions*, arXiv:2012.04666.

[45] Sarang Gopalakrishnan and Michael J. Gullans, *Entanglement and Purification Transitions in Non-Hermitian Quantum Mechanics*, Phys. Rev. Lett. **126**, 170503 (2021).

[46] Xhek Turkeshi, *Measurement-Induced Criticality as a Data-Structure Transition*, arXiv:2101.06245.

[47] Yimu Bao, Soonwon Choi, and Ehud Altman, *Symmetry Enriched Phases of Quantum Circuits*, Ann. Phys. (Amsterdam) **435**, 168618 (2021).

[48] Maxwell Block, Yimu Bao, Soonwon Choi, Ehud Altman, and Norman Y. Yao, *Measurement-Induced Transition in Long-Range Interacting Quantum Circuits*, Phys. Rev. Lett. **128**, 010604 (2022).

[49] Gregory S. Bentsen, Subhayan Sahu, and Brian Swingle, *Measurement-Induced Purification in Large-N Hybrid Brownian Circuits*, Phys. Rev. B **104**, 094304 (2021).

[50] Crystal Noel, Pradeep Niroula, Daiwei Zhu, Andrew Risinger, Laird Egan, Debopriyo Biswas, Marko Cetina, Alexey V. Gorshkov, Michael J. Gullans, David A. Huse, and Christopher Monroe, *Measurement-Induced Quantum Phases Realized in a Trapped-Ion Quantum Computer*, Nat. Phys. **18**, 760 (2022).

[51] Aaron J. Friedman, Amos Chan, Andrea De Luca, and J. T. Chalker, *Spectral Statistics and Many-Body Quantum Chaos with Conserved Charge*, Phys. Rev. Lett. **123**, 210603 (2019).

[52] Tibor Rakovszky, Frank Pollmann, and C. W. von Keyserlingk, *Sub-Ballistic Growth of Rényi Entropies due to Diffusion*, Phys. Rev. Lett. **122**, 250602 (2019).

[53] Yichen Huang, *Dynamics of Rényi Entanglement Entropy in Diffusive Qudit Systems*, IOP SciNotes **1**, 035205 (2020).

[54] Tianci Zhou and Andreas W. W. Ludwig, *Diffusive Scaling of Rényi Entanglement Entropy*, Phys. Rev. Research **2**, 033020 (2020).

[55] Tibor Rakovszky, Frank Pollmann, and C. W. von Keyserlingk, *Comment on "Entanglement Growth in Diffusive Systems,"* arXiv:2010.07969.

[56] Marko Žnidarič, *Entanglement Growth in Diffusive Systems*, Commun. Phys. **3**, 1 (2020).

[57] Fergus Barratt, Utkarsh Agrawal, Sarang Gopalakrishnan, David A. Huse, Romain Vasseur, and Andrew C. Potter, *Field Theory of Charge Sharpening in Symmetric Monitored Quantum Circuits*, arXiv:2111.09336.

[58] Since the unitaries acting on the qudits are random, the randomizing measurement basis is superfluous.

[59] Alexandre Blais, Arne L. Grimsmo, S. M. Girvin, and Andreas Wallraff, *Circuit Quantum Electrodynamics*, Rev. Mod. Phys. **93**, 025005 (2021).

[60] The ensemble-averaged $\rho(t)$ resulting from maximally random, local, open-systems dynamics is indistinguishable from an infinite temperature state over distances $\sim t$.

[61] This can seen by the central limit theorem as follows: assuming each measurement outcome to be independent, the statistical error in the outcomes of the measurement of charge density goes as $1/\sqrt{\mathcal{N}_M}$. To distinguish the states with global charge N and $N-1$, we require this error to become smaller than $\sim 1/L$. This gives $\mathcal{N}_M \sim L^2$.

[62] Yichen Huang, *Dynamics of Rényi Entanglement Entropy in Diffusive Qudit Systems*, IOP SciNotes **1**, 035205 (2020).

[63] Though other quantities such as $\log[e^{-S_n}]$ are dominated by rare dead-region contributions and do exhibit $\sqrt{t}$ growth due to rare dilute measurement locations. The parametrically strong discrepancy between the average purity and the average Rényi entropies is also seen numerically in our statistical model approach (Sec. V).

[64] To obtain a uniform distribution over U(2) we must pick $\alpha, \psi, \chi \in [0, 2\pi)$ and $\xi \in [0, 1]$ uniformly and compute $\phi = \arcsin\sqrt{\xi}$.

[65] In the absence of a conservation law, it has been shown that the probes we have used for the entanglement transition ($\mathcal{I}_{3,n}$ and $[S_{1,E}]$) have weak finite size drifts in Clifford circuits [28] by examining small and large system sizes.

[66] Patrick Hayden, Sepehr Nezami, Xiao Liang Qi, Nathaniel Thomas, Michael Walter, and Zhao Yang, *Holographic Duality from Random Tensor Networks*, J. High Energy Phys. 11 (2016) 009.

[67] Romain Vasseur, Andrew C. Potter, Yi Zhuang You, and Andreas W. W. Ludwig, *Entanglement Transitions from Holographic Random Tensor Networks*, Phys. Rev. B **100**, 134203 (2019).

[68] DWs are restricted by unitarity to only make certain "turns" (see Ref. [10] for details). For example, for $p = 0$, this leads to a unique DW where the DW follows a "light cone." For $p > 0$ one can still have many degenerate paths [17].

[69] Any difference in the vertex elements will lead to the creation of DW which are suppressed as $\mathcal{O}(1/d)$ and whose contribution goes to zero as $d \to \infty$.

[70] Note that the DW permutation element $(1\ldots n)^{\otimes k}$ has $k+1$ cycles and each cycle can follow an independent path (to the leading order) [10]. However, this subtlety will not change the final result about the minimal cut, but only leads to fluctuations contributing subleading logarithmic corrections (for $p > 0$).

[71] Note that this description of the $d \to \infty$ differs from that of Ref. [20]. There the measurement locations $\sum_{\mathbf{x}}$ were averaged over directly in the partition function, in an annealed way, while we chose here to keep the measurement locations as quenched disorder. Our approach predicts a minimal cut picture consistent with Ref. [14]. We leave a discussion of the validity of the replica trick in this limit to future work.

[72] Ulrich Schollwöck, *The Density-Matrix Renormalization Group in the Age of Matrix Product States*, Ann. Phys. (Amsterdam) **326**, 96 (2011).

[73] Frozen in the sense that there is not much quantum superposition of different charge configurations.

[74] Zack Weinstein, Yimu Bao, and Ehud Altman, *Measurement-Induced Power Law Negativity in an Open Monitored Quantum Circuit*, arXiv:2202.12905.

[75] Matthew Fisher, *Duality in Low Dimensional Quantum Field Theories*, in *Strong Interactions in Low Dimensions* (Springer, New York, 2004), pp. 419–438.

[76] Andrew C. Potter and Romain Vasseur, *Symmetry Constraints on Many-Body Localization*, Phys. Rev. B **94**, 224206 (2016).

[77] Xie Chen, Zheng Cheng Gu, Zheng Xin Liu, and Xiao Gang Wen, *Symmetry Protected Topological Orders and the Group Cohomology of Their Symmetry Group*, Phys. Rev. B **87**, 155114 (2013).

[78] Xie Chen, Zheng Cheng Gu, Zheng Xin Liu, and Xiao Gang Wen, *Symmetry-Protected Topological Orders in Interacting Bosonic Systems*, Science **338**, 1604 (2012).

[79] Xie Chen, Yuan Ming Lu, and Ashvin Vishwanath, *Symmetry-Protected Topological Phases from Decorated Domain Walls*, Nat. Commun. **5**, 3507 (2014).

[80] Youjin Deng and Henk W. J. Blöte, *Simultaneous Analysis of Several Models in the Three-Dimensional Ising Universality Class*, Phys. Rev. E **68**, 036125 (2003).